

Three dimensional hierarchical mixed finite element approximations with enhanced primal variable accuracy

Douglas A. Castro^a, Philippe R.B. Devloo^{b,*}, Agnaldo M. Farias^c, Sônia M. Gomes^d,
Denise de Siqueira^e, Omar Durán^f

^a Universidade Federal do Tocantins - Campus Gurupi, TO, Brazil

^b Faculdade de Engenharia Civil Arquitetura e Urbanismo - Universidade Estadual de Campinas, Campinas, SP, Brazil

^c Departamento de Matemática - IFNMG, Salinas, MG, Brazil

^d Instituto de Matemática Estatística e Computação Científica - Universidade Estadual de Campinas, Campinas, SP, Brazil

^e Departamento de Matemática, UTFPR, Curitiba, PR, Brazil

^f Faculdade de Engenharia Mecânica - Universidade Estadual de Campinas, Campinas, SP, Brazil

Received 5 February 2016; received in revised form 16 March 2016; accepted 31 March 2016

Available online 4 May 2016

Abstract

There are different possibilities of choosing balanced pairs of approximation spaces for dual (flux) and primal (pressure) variables to be used in discrete versions of the mixed finite element method for elliptic problems arising in fluid simulations. Three cases shall be studied and compared for discretized three dimensional formulations based on tetrahedral, hexahedral and prismatic meshes. The principle guiding the constructions is the property that the divergence of the dual space and the primal approximation space should coincide, while keeping the same order of accuracy for the flux variable and varying the accuracy order of the primal variable. There is the classic case of BDM_k spaces based on tetrahedral meshes and polynomials of total degree k for the dual variable, and $k - 1$ for the primal variable, showing stable simulations with optimal convergence rates of orders $k + 1$ and k , respectively. Another case is related to RT_k and $BDFM_{k+1}$ spaces for hexahedral and tetrahedral meshes, respectively, but holding for prismatic elements as well. It gives identical approximation order $k + 1$ for both primal and dual variables, an improvement in accuracy obtained by increasing the degree of primal functions to k , and by enriching the dual space with some properly chosen internal shape functions of degree $k + 1$, while keeping degree k for the border fluxes. A new type of approximation is proposed by further incrementing the order of some internal flux functions to $k + 2$, and matching primal functions to $k + 1$ (higher than the border fluxes of degree k). Thus, higher convergence rate of order $k + 2$ is obtained for the primal variable. Using static condensation, the global condensed system to be solved in all the cases has same dimension (and structure), which is proportional to the space dimension of the border fluxes for each element geometry. Illustrating results comparing the three different space configurations are presented for simulations based on hierarchical high order shape functions for $\mathbf{H}(\text{div})$ -conforming spaces,

* Corresponding author. Tel.: +55 19 35212396.

E-mail addresses: dacastro@mail.uft.edu.br (D.A. Castro), phil@fec.unicamp.br (P.R.B. Devloo), agnaldofarias.mg@gmail.com (A.M. Farias), soniag@ime.unicamp.br (S.M. Gomes), denisesiqueira@utfpr.edu.br (D. de Siqueira), omar@dep.fem.unicamp.br (O. Durán).

which are specially constructed for affine tetrahedral, hexahedral and prismatic meshes. Expected convergence rates are obtained for the flux, pressure and divergence variables.

© 2016 Elsevier B.V. All rights reserved.

Keywords: Finite elements; $\mathbf{H}(\text{div})$ spaces; Mixed formulation; Approximation space configurations; Convergence rates; 3D meshes

1. Introduction

Mixed finite element methods have the ability to provide accurate and locally conservative fluxes, an advantage over standard H^1 -finite element discretizations [1]. They are based on simultaneous approximations of the primal (pressure) and dual (flux) variables, involving two kinds of approximation spaces. In addition to $\mathbf{H}(\text{div})$ -conforming approximation spaces for the dual variable, with continuous normal components over element interfaces, the primal variable is usually represented in discontinuous finite element spaces.

Since the pioneering work by Raviart and Thomas [2] in 1977, different constructions of $\mathbf{H}(\text{div})$ (or $\mathbf{H}(\text{curl})$) approximation spaces have been proposed in [3–7]. Recently, several other papers have appeared in the literature due to increasing interest on this subject. In some contexts the vector basis functions are constructed directly on the physical element, but when it comes to solving practical problems in complex domains, shape functions are defined on the master element and then they are transformed to the elements of the partition using Piola transformations. Constructions of hierarchical high order spaces in [8–13] are based on the properties of the De Rham complex, which are essential in the stability proof. There is also the methodology based on finite element exterior calculus [14,15] that can be used for the construction of stable discretizations of a variety of problems in a unified framework, which is used in [16] for the implementation of some classic simplicial space configurations in the FEniCS software. In [17] and [18] innovative families of spaces are presented for quadrilateral meshes in order to improve convergence rates in flux divergence, a common deficiency for general elements of other constructions.

The main purpose of this article is to analyse and compare the performance of different ways of choosing balanced pairs of approximation spaces (\mathbf{V}_h, U_h) , for dual and for primal variables, based on tetrahedral, hexahedral and prismatic meshes, to be used in discrete versions of the mixed finite element method for three dimensional elliptic problems. The methods share the following basic characteristics:

1. The flux approximation spaces \mathbf{V}_h shall be spanned by a hierarchy of vectorial shape functions, which are organized into two classes: the shape functions of interior type, with vanishing normal components over all element faces, and the shape functions associated to the element faces.
2. In all the cases, as in the de Rham complex, the aim is to verify the discrete exact sequence property

$$\nabla \cdot \mathbf{V}_h = U_h, \quad (1)$$

in order to obtain stable results with optimal L^2 -error convergence orders, which are dictated by the degree of the complete set of polynomials used to form the corresponding approximation spaces.

For the classic Brezzi–Douglas–Marini (BDM_k) spaces applied to triangular elements [3], and their generalization to tetrahedral geometries by Nédélec [5], stable approximations can be obtained with spaces of type $\mathbf{P}_k P_{k-1}$, which are based on complete scalar polynomials of total degree $k - 1$ for approximations of the primal variable, and of total degree k for the components of $\mathbf{H}(\text{div})$ approximations of the dual variable. In these cases, property (1) holds, resulting in stable simulations with optimal convergence rates, in the L^2 -norm, of orders $k + 1$ and k for dual and primal variables, respectively.

For hexahedral, and prismatic 3D geometries, and also for quadrilateral 2D meshes, approximation spaces of type $\mathbf{P}_k P_{k-1}$ cannot verify property (1), and thus they are not consistent. However, approximation spaces of type $\mathbf{P}_k^* P_k$ are possible to construct for these geometries, and also for triangles, quadrilaterals, and tetrahedra as well, with optimal convergence rates of order $k + 1$ for both dual and primal variables. The principle for the construction of \mathbf{P}_k^* type of flux approximations is to enrich the dual space \mathbf{P}_k with some properly chosen internal shape functions of degree $k + 1$, while keeping degree k for the border fluxes. This type of space configuration was first introduced by Raviart–Thomas (RT_k) for quadrilateral geometries, and its generalization to three dimension in [4]. This idea has also being used for the construction of the classic Brezzi–Douglas–Fortin–Marini ($BDFM_{k+1}$) elements for triangular

and tetrahedral geometries, where BDM_k spaces are enriched with internal functions in \mathbf{P}_{k+1} , but restricting the face shape functions to those ones whose normal components are total polynomials of degree k on element interfaces [7,1]. Nédélec prismatic elements introduced in [5] are also derived by a similar principle, but they contain less internal vectorial functions than in the $\mathbf{P}_k^* P_k$ space configuration proposed in the present paper.

A new type of approximation space configuration, denoted by $\mathbf{P}_k^{**} P_{k+1}$, is proposed and tested in the present article for the three cases of mesh geometry. The notation \mathbf{P}_k^{**} refers to $\mathbf{H}(\text{div})$ -approximation spaces constructed out of the spaces of type \mathbf{P}_{k+1}^* by keeping only those face functions whose normal components on element interfaces come from polynomials of degree at most k . In the $\mathbf{P}_k^{**} P_{k+1}$ context, optimal convergence rates of order $k + 1$ in the flux variable and $k + 2$ in the primal variable are obtained for all element geometries. This result is important because it demonstrates that the error rate of convergence for the primal variable is one order higher than all $\mathbf{H}(\text{div})$ -conforming approximation spaces documented so far. It should be observed that these higher convergence rates for the primal variable are consistent with (theoretical) convergence rates observed in Multiscale Hybrid Methods [19], where refined H^1 approximations are used in the interior of the elements. Instead, we propose to use higher order mixed finite element approximations in the interior of the elements while keeping the order of border flux functions. Enrichment of the flux space with internal shape functions has also been used in [17] for accuracy improvement in the L^2 -norm of the divergence of the dual variable when applied to trapezoidal meshes.

Another purpose of the present paper is to emphasize the importance of the key property common to these space configurations concerning the use of static condensation. For $\mathbf{P}_k^{**} P_{k+1}$ and $\mathbf{P}_k^* P_k$ frameworks, as well as for the $\mathbf{P}_k P_{k-1}$ setting in case of tetrahedral (and triangular) elements, the dimension (and structure) of the global condensed matrices to be solved is the same, which is proportional to the dimension of the space of border fluxes for each geometry. Consequently, for each accuracy order for the flux variable, at least two approximation space configurations are available for all mesh geometries, showing proportional implementation costs, but with the possibility of choosing the $\mathbf{P}_k^{**} P_{k+1}$ framework with higher accuracy rate for the primal variable. We show that the static condensation technique makes these $\mathbf{H}(\text{div})$ -conforming approximations competitive with H^1 -conforming approximations if the errors are charted as a function of the size of the global condensed systems of equations to be solved.

Convergence rates and the effect of static condensation for the three kinds of space configurations are illustrated for simulations based on affine meshes and approximation spaces based on innovative hierarchical high order shape functions for $\mathbf{H}(\text{div})$ -conforming spaces. As explained in Appendix A, the methodology for the construction of these vectorial shape functions is an extension to affine tetrahedral, hexahedral and prismatic geometries of previous developments in 2D geometries [20]. The principle is to choose appropriate constant vector fields, based on the geometry of each element of a given partition of the computational region Ω , which are multiplied by an available set of H^1 hierarchical scalar basis functions. This strategy produces shape functions for vectorial polynomial spaces \mathbf{P}_k in each physical element that can easily be assembled to generate approximations subspaces \mathbf{V}_h with continuous normal components over the elements interfaces, the property that characterizes $\mathbf{H}(\text{div})$ -conforming functions. This property is obtained as a consequence of the particular properties verified by the proposed vector fields, and of the continuity of the scalar shape functions used in their construction. This fact facilitates the combination of different element geometries in a single mesh and the design of hp -adaptive strategies for $\mathbf{H}(\text{div})$ -conforming approximations, as described in [21] for 2D quadrilateral and triangular affine meshes. The vectorial shape functions spanning \mathbf{P}_k are used to define the three kinds of space configurations $\mathbf{P}_k P_{k-1}$, $\mathbf{P}_k^* P_k$, and $\mathbf{P}_k^{**} P_{k+1}$ satisfying the basic properties described before.

The proposed systematic way of building the shape functions allowed us not only to implement and validate $\mathbf{H}(\text{div})$ -conforming approximations for the complete family of three dimensional finite element topologies (excluding the pyramid), but also helped us to implement the static condensation procedure for all space configurations in a unified way, and to understand the natural way to increase the polynomial order of internal degrees of freedom in the $\mathbf{P}_k^{**} P_{k+1}$ framework, obtaining higher convergence rates for the primal variable.

Despite the variety of stable $\mathbf{H}(\text{div})$ -conforming space configurations available in the literature, their implementations are much more complex than for H^1 -conforming element schemes. The assemblage and implementation of $\mathbf{H}(\text{div})$ bases, and the evaluation of the corresponding variational formulations present a challenge in terms of code complexity. This is a reason for the fact that there exist few computational environments available to the scientific finite element community which implement approximation spaces for the complete family of finite element topologies. All the implementations of the present paper are performed in the object-oriented scientific computational environment NeopZ [22]. This is a general finite element approximation software organized by modules for a broad classes

of technologies, incorporating a variety of element geometries, variational formulations, and approximation spaces (e.g. continuous, discontinuous, $\mathbf{H}(\text{div})$, and others). It allows the user to apply hp -strategies by locally choosing the mesh refinement, and the order of approximation. NeoPZ is integrated with pthreads, and thread building blocks for efficient execution on multi core computers. Multiphysics simulations can also be implemented by combining different approximation spaces into a coupled system of equations [23], a procedure that facilitates the implementation of mixed formulations based on different approximations spaces for dual and primal variables. In fact, the current proposed methodology for the construction of $\mathbf{H}(\text{div})$ -conforming functions, described in Appendix, is designed having in mind the resources provided by NeoPZ, where the required hierarchical high order continuous scalar basis functions are already implemented for regular or irregular hp -meshes [24,25].

The paper is organized as follows. The mixed element formulation for a model Poisson problem is set in Section 2. The three proposed approximation space configurations are described in 3, where the static condensation strategy is stated for them. A unified script for the construction of projections commuting the de Rham diagram is presented in Appendix B for all the space configurations and element geometries. Based on these projections, classic techniques can be used to obtain the expected error estimates for approximate solutions by the mixed method based on all analysed space configurations, as described in Section 3.2. The simulation results using different pairs for $\mathbf{H}(\text{div}) - L^2$ mixed finite element spaces to approximate the model problem defined in Section 2, with known analytical solution, are discussed in Section 4 for tetrahedral, hexahedral, and prismatic affine meshes. In Section 5, the robustness of the approximation frameworks is evaluated in order to confirm the predicted convergence rates also for non-uniform zig-zag meshes combining hexahedral and prismatic affine elements, and for irregular affine tetrahedral meshes. Section 6 gives the final conclusions of the article. The methodology for the construction of the vectorial $\mathbf{H}(\text{div})$ bases implemented in NeoPZ is described in Appendix A, for affine tetrahedral, hexahedral, and prismatic partitions.

2. Mixed finite element method for a model problem

Consider a model Poisson problem expressed as:

$$\boldsymbol{\sigma} = -\nabla u \quad \text{in } \Omega, \quad (2)$$

$$\nabla \cdot \boldsymbol{\sigma} = f \quad \text{in } \Omega, \quad (3)$$

$$u = 0 \quad \text{in } \partial\Omega, \quad (4)$$

where $\Omega \subset \mathbb{R}^3$ is the computational domain with Lipschitz boundary $\partial\Omega$.

The classical mixed formulation for problem (2)–(4) requires the space

$$\mathbf{H}(\text{div}, \Omega) = \left\{ \mathbf{q} \in \left[L^2(\Omega) \right]^3; \nabla \cdot \mathbf{q} \in L^2(\Omega) \right\}.$$

As studied in [1], the mixed formulation for problem (2)–(4) is given as: find $(\boldsymbol{\sigma}, u) \in (\mathbf{H}(\text{div}, \Omega) \times L^2(\Omega))$ such that

$$\int_{\Omega} \boldsymbol{\sigma} \cdot \mathbf{q} \, d\Omega - \int_{\Omega} u \nabla \cdot \mathbf{q} \, d\Omega = 0, \quad (5)$$

$$\int_{\Omega} \nabla \cdot \boldsymbol{\sigma} \varphi \, d\Omega = \int_{\Omega} f \varphi \, d\Omega, \quad (6)$$

for all $\mathbf{q} \in \mathbf{V} = \mathbf{H}(\text{div}, \Omega)$, and $\varphi \in U = L^2(\Omega)$. This problem can be expressed in the saddle point form

$$a(\boldsymbol{\sigma}, \mathbf{q}) + b(\mathbf{q}, u) = 0,$$

$$b(\boldsymbol{\sigma}, \varphi) = \ell(\varphi),$$

where $a(\boldsymbol{\sigma}, \mathbf{q}) = \int_{\Omega} \boldsymbol{\sigma} \cdot \mathbf{q} \, d\Omega$, $b(\mathbf{q}, u) = - \int_{\Omega} u \nabla \cdot \mathbf{q} \, d\Omega$, and $\ell(\varphi) = - \int_{\Omega} f \varphi \, d\Omega$.

In typical $\mathbf{H}(\text{div})$ -conforming discretized versions of the mixed formulation, approximate solutions for dual $\boldsymbol{\sigma}$ and primal u variables are searched in finite dimensional subspaces $\mathbf{V}_h \subset \mathbf{V}$ and $U_h \subset U$, and the system of variational equations (5)–(6) is enforced by test functions $\mathbf{q} \in \mathbf{V}_h$ and $\varphi \in U_h$. In matrix form, the discrete version of system

(5)–(6) can be written as

$$\begin{pmatrix} A & B^T \\ B & 0 \end{pmatrix} \begin{pmatrix} \sigma_h \\ u_h \end{pmatrix} = \begin{pmatrix} 0 \\ -f_h \end{pmatrix}, \quad (7)$$

where the matrices A and B correspond to discrete versions of the bilinear forms $a(\sigma, \mathbf{q})$ and $b(\sigma, \varphi)$. The vectors σ_h and u_h denote the dual and the primal degrees of freedom, and f_h is associated to the L^2 projection of the forcing term on U_h .

3. Types of approximation space configurations

The main goal of the paper is to illustrate different possibilities for the resolution of the model problem (3)–(4) by the mixed formulation (5)–(6), with varying approximation space configurations (\mathbf{V}_h, U_h) , based on regular meshes $\Gamma_h = \{K\}$, with affine elements of characteristic length h , to produce different orders of accuracy for the primal variable, while keeping fixed the order of accuracy for the dual variable. The elements can be of tetrahedral, hexahedral or prismatic geometry.

For the definitions of the approximation spaces, some general aspects must be taken into account:

- There are spaces $P_k(K)$ of polynomials restricted to K used in the construction of scalar approximations for the primal variable, where the index k refers to polynomial degree. For tetrahedra, the polynomials in $P_k(K)$ have total degree k , and for hexahedra, they have maximum degree k in each coordinate. For prismatic elements, $P_k(K)$ is formed by polynomials of total degree k in the triangular faces and of maximum degree k in the complementary direction. Vectorial polynomial spaces $\mathbf{P}_k(K)$ mean that the components of the vectorial shape functions are obtained from polynomials in $P_k(K)$.
- The approximation subspaces $U_h \subset L^2(\Omega)$ for the primal variable are piecewise formed as $u|_K = u_K$, for $K \in \Gamma_h$, without any continuity constraint.
- The approximation subspaces $\mathbf{V}_h \subset \mathbf{H}(\text{div}, \Omega)$ are formed by functions \mathbf{q} piecewise defined over the elements of Γ_h by local functions $\mathbf{q}_K := \mathbf{q}|_K$, which are spanned by hierarchical vectorial bases in $\mathbf{H}(\text{div}, K)$. The shape functions Φ in those bases can be classified as of interior type, with vanishing normal components over all element faces. Otherwise, Φ is classified as of face type, with normal components vanishing over all other faces not associated to it.
- In all the cases, the choices of the approximation spaces are guided by the property that the image of \mathbf{V}_h by the divergence operator coincides with U_h , as stated in Eq. (1).

Three kinds of space configurations for (\mathbf{V}_h, U_h) shall be considered.

Approximations of type $\mathbf{P}_k P_{k-1}$

For this configuration, the dual approximation space of type \mathbf{P}_k is based on complete vector valued polynomials of degree k , and the primal approximation space of type P_{k-1} is based on the complete scalar valued polynomials of degree $k - 1$. However, it is well known that this kind of space configuration satisfying property (1) can only be valid for triangular and tetrahedral meshes, corresponding to the classic BDM_k elements, for which L^2 -error convergence of orders $k + 1$ and k , for dual and primal variables can be obtained.

Approximations of type $\mathbf{P}_k^* P_k$

For all the geometries, another type of space configuration $(\mathbf{V}_k^{T_h}, U_k^{T_h})$ can be considered. Guided by the verification of property (1), the dual approximations in $\mathbf{V}_k^{T_h}$ are said to be of \mathbf{P}_k^* type if they are locally spanned by the face functions of $\mathbf{P}_k(K)$ type, and by the internal shape functions of $\mathbf{P}_{k+1}(K)$ defined by vectorial polynomials of degree $k + 1$ whose divergence is included in the primal approximation space of type $P_k(K)$. Since the incomplete dual approximation space of type \mathbf{P}_k^* only involves the complete vector valued polynomials of degree k , in simulations using $\mathbf{P}_k^* P_k$ configurations the expected L^2 -error convergence rates are of order $k + 1$ for both dual and primal variables. This is the type of RT_k space configuration for quadrilateral geometries, and their generalization to hexahedral partitions in [4], and of $BDFM_{k+1}$ elements for triangular or tetrahedral elements. For prismatic elements, $\mathbf{P}_k^*(K)$ contain Nédélec's elements $N_k(K)$ [5].

Approximations of type $\mathbf{P}_k^{**} P_{k+1}$

The construction of flux approximation spaces of type \mathbf{P}_k^{**} consists in adding to the complete vector valued spaces of type \mathbf{P}_k those interior shape functions of $\mathbf{P}_{k+1}^*(K)$ defined by vectorial polynomials of degree $k+2$ whose divergence is included in the primal approximation space of type $P_{k+1}(K)$. Therefore, in $\mathbf{P}_k^{**}(K)$ the face shape functions are still obtained by polynomials of degree $\leq k$, but some of the internal shape functions may be obtained from polynomials of degree up to $k+2$. As in the previous case, here the verification of property (1) is the basic principle guiding the definition of the pair of approximation spaces. For this setting, $\mathbf{P}_k^{**}(K)$ contains only the complete vector valued approximations $\mathbf{P}_k(K)$, the L^2 -error convergence rate of order $k+1$ is expected for the dual variable. However, for the primal variable a higher order $k+2$ may be reached. To our knowledge, space configurations $\mathbf{P}_k^{**} P_{k+1}$, which are valid for all element geometries, are new in the literature.

3.1. Static condensation

When using these kinds of approximations in the mixed formulation, the degrees of freedom of the flux may be organized in the form σ_{ih} , σ_{eh} , where σ_{ih} and σ_{eh} refer to internal and or external (face) components of the flux, respectively. For the pressure, a scalar value is denoted by u_{0h} , and u_{ih} are the values of the pressure approximation except u_{0h} . Thus, the matrix representation (7) can be expressed in the form

$$\left(\begin{array}{cc|cc} A_{ii} & B_{ii}^T & B_{ie}^T & A_{ie} \\ B_{ii} & 0 & 0 & B_{ie} \\ \hline B_{ie} & 0 & 0 & B_{ee} \\ A_{ei} & B_{ie}^T & B_{ee}^T & A_{ee} \end{array} \right) \begin{pmatrix} \sigma_{ih} \\ u_{ih} \\ u_{0h} \\ \sigma_{eh} \end{pmatrix} = \begin{pmatrix} 0 \\ -f_{ih} \\ -f_{0h} \\ 0 \end{pmatrix}.$$

Then, static condensation may be applied by eliminating the internal degrees of freedom σ_{ih} and u_{ih} , to get a condensed system in terms of σ_{eh} and u_{0h} .

On each element, the dimension of the static condensed matrix is determined by the number of degrees of freedom of the face components σ_{eh} plus one, which coincides for the approximations spaces of types $\mathbf{P}_k P_{k-1}$, $\mathbf{P}_k^* P_k$, and $\mathbf{P}_k^{**} P_{k+1}$.

For the numerical tests presented in the next section, flux approximations are obtained from vectorial shape functions forming bases \mathbf{B}_k^K of type \mathbf{P}_k for affine tetrahedral, hexahedral, and prismatic partitions. Table 1 presents the numbers of vectorial shape functions in \mathbf{B}_k^K , as well as the number of the corresponding shape functions of type \mathbf{P}_k^* and \mathbf{P}_k^{**} derived from them.

As described in Appendix A, these hierarchical bases are of the form

$$\mathbf{B}_k^K = \underbrace{\left\{ \Phi^{F,a}, \Phi^{F,l,n}, \Phi^{F,n_1,n_2} \right\}}_{\text{face functions}} \cup \underbrace{\left\{ \Phi^{K,l,n}, \Phi_{(1)}^{K,F,n_1,n_2}, \Phi_{(2)}^{K,F,n_1,n_2}, \Phi_{(1)}^{K,n_1,n_2,n_3}, \Phi_{(2)}^{K,n_1,n_2,n_3}, \Phi_{(3)}^{K,n_1,n_2,n_3} \right\}}_{\text{internal functions}}, \quad (8)$$

where F indicates faces of the element K , a and l being their vertices and edges. The principle in the definition of these vectorial shape functions is to choose appropriate constant vector fields \mathbf{v} , based on the geometry of each element K , which are multiplied by an available set of H^1 hierarchical scalar basis functions φ . The scalar shape functions are classified in terms of vertex, edge, face or internal types. The indexes n or n_i determine the degree of the polynomials used in their construction, as described in [24], for conforming meshes and uniform distribution of k , and in [25] for hp -adapted meshes.

3.2. Error estimates

As for the unified error analysis described in [1], for a variety of approximation settings, let us denote by $\mathbf{M}(K)$ anyone of the local approximation spaces of type $\mathbf{P}_k(K)$, $\mathbf{P}_k^*(K)$ or $\mathbf{P}_k^{**}(K)$, restricted to elements $K \in \Gamma_h$. As

Table 1

Number of vectorial shape functions in the bases of type \mathbf{P}_k , \mathbf{P}_k^* and \mathbf{P}_k^{**} for tetrahedral (\mathcal{T}_e), hexahedral (\mathcal{H}), and prismatic (\mathcal{P}_r) elements.

Element	Type	Face	Internal	Total
\mathcal{T}_e	\mathbf{P}_k	$2(k+1)(k+2)$	$\frac{1}{2}(k^2-1)(k+2)$	$\frac{1}{2}(k+1)(k+2)(k+3)$
	\mathbf{P}_k^*	$2(k+1)(k+2)$	$\frac{1}{2}k(k+2)(k+3)$	$\frac{1}{2}(k+2)[k(k+3)+4(k+1)]$
	\mathbf{P}_k^{**}	$2(k+1)(k+2)$	$\frac{1}{2}(k+1)(k+3)(k+4)$	$\frac{1}{2}(k+1)[(k+3)(k+4)+4(k+2)]$
\mathcal{H}	\mathbf{P}_k	$6(k+1)^2$	$3(k-1)(k+1)^2$	$3(k+1)^3$
	\mathbf{P}_k^*	$6(k+1)^2$	$3k(k+1)^2$	$3(k+1)^2(k+2)$
	\mathbf{P}_k^{**}	$6(k+1)^2$	$3(k+1)(k+2)^2$	$3(k+1)[6+k(k+6)]$
\mathcal{P}_r	\mathbf{P}_k	$(k+1)(4k+5)$	$\frac{1}{2}(k^2-1)(3k+4)$	$\frac{3}{2}(k+1)^2(k+2)$
	\mathbf{P}_k^*	$(k+1)(4k+5)$	$\frac{1}{2}k^2(3k+5)+7k-2$	$\frac{1}{2}k^2(3k+13)+16k+3$
	\mathbf{P}_k^{**}	$(k+1)(4k+5)$	$\frac{1}{2}(k+1)^2(3k+8)+7k+5$	$\frac{1}{2}k^2(3k+22)+\frac{5}{2}k+14$

observed, $\mathbf{P}_k(K) \subseteq \mathbf{M}(K)$ but $\mathbf{P}_{k+1}(K) \not\subseteq \mathbf{M}(K)$. Let also consider the spaces $D(K) = \nabla \cdot \mathbf{M}(K)$. Precisely, for tetrahedra, $D(K) = P_{k-1}(K)$ for the BDM_k spaces, where $\mathbf{M}(K) = \mathbf{P}_k(K)$. For all geometries, $D(K) = P_k(K)$ for spaces $\mathbf{M}(K) = \mathbf{P}_k^*(K)$, and $D(K) = P_{k+1}(K)$ when $\mathbf{M}(K) = \mathbf{P}_k^{**}(K)$.

Consider pairs of spaces $\mathbf{V}_h \times U_h$ defined by local approximations

$$\begin{aligned} \mathbf{V}_h &= \{\mathbf{q} \in \mathbf{H}(\text{div}, \Omega); \mathbf{q}|_K \in \mathbf{M}(K), K \in \Gamma_h\}, \\ U_h &= \left\{u \in L^2(\Omega); u|_K \in D(K), K \in \Gamma_h\right\}. \end{aligned}$$

By construction, the crucial property $\nabla \cdot \mathbf{V}_h = U_h$ holds. Therefore, classic techniques can be used for stability and error analyses of approximate solutions $(\sigma_h, u_h) \in \mathbf{V}_h \times U_h$ of the mixed formulation based on such spaces, for which it is necessary to define projections

$$\Lambda_h \times \Pi_h : \mathbf{H}^1(\Omega) \times L^2(\Omega) \rightarrow \mathbf{V}_h \times U_h$$

commuting the de Rham diagram

$$\begin{array}{ccc} \mathbf{H}^1(\Omega) & \xrightarrow{\nabla \cdot} & L^2(\Omega) \\ \downarrow \Lambda_h & & \downarrow \Pi_h, \\ \mathbf{V}_h & \xrightarrow{\nabla \cdot} & U_h \end{array}$$

where the space $\mathbf{H}^1(\Omega) \subset \mathbf{H}(\text{div}, \Omega)$, denoting the vector analogue of $H^1(\Omega)$, is taken in order to guarantee L^2 -integrable normal traces $\mathbf{q} \cdot \boldsymbol{\eta}_K|_{\partial K}$ over element boundaries.

For $z \in L^2(\Omega)$, the projection $\Pi_h z$ on the scalar approximation space U_h is usually taken as the L^2 -projection such that

$$\int_{\Omega} (z - \Pi_h z) \varphi d\Omega = 0, \quad \forall \varphi \in U_h.$$

For smooth vectorial functions $\mathbf{q} \in \mathbf{H}(\text{div}, \Omega)$, the projection $\Lambda_h \mathbf{q}$ can be defined in terms of local projections by

$$\Lambda_h \mathbf{q}|_K = \lambda_K \mathbf{q}, \quad \forall K \in \Gamma_h,$$

where $\lambda_K : \mathbf{H}^1(K) \rightarrow \mathbf{M}(K)$ should verify the local de Rham property

$$\nabla \cdot \lambda_K \mathbf{q} = \pi_K \nabla \cdot \mathbf{q}, \quad (9)$$

where π_K denotes the L^2 -projection on $D(K)$.

Based on such properties, Proposition 1.2, p. 139 in [1] establishes convergence rates of the form

$$\|\sigma - \sigma_h\|_0 = O(h^{k+1}), \quad (10)$$

$$\|u - u_h\|_0 = O(h^s), \quad (11)$$

with $s = k$ for BDM_k spaces of type $\mathbf{P}_k P_{k-1}$ for tetrahedral partitions, and $s = k + 1$ when spaces of type $\mathbf{P}_k^* P_k$ are used, for tetrahedral $BDFM_{k+1}$ elements, and hexahedral Raviart–Thomas elements RT_k . Here $\|\cdot\|_0$ denotes the usual L^2 -norms of vectorial or scalar spaces. In addition, because the meshes are supposed to be affine, and $\nabla \cdot \boldsymbol{\sigma}_h$ results to be the $L^2(\Omega)$ -projection of $\nabla \cdot \boldsymbol{\sigma}$ on U_h , then the divergence error $\|\nabla \cdot \boldsymbol{\sigma} - \nabla \cdot \boldsymbol{\sigma}_h\|_{L^2(\Omega)}$ has the same accuracy rate as for the error in u .

Based on the properties deduced in Appendix B for local projections $\lambda_K \mathbf{q}$ commuting the local de Rham diagrams, similar convergence rates hold for the new spaces of type $\mathbf{P}_k^* P_k$ based on prisms, with the error in u of order $s = k + 1$. Furthermore, for $\mathbf{P}_k^{**} P_{k+1}$ space configurations, enhanced accuracy orders $s = k + 2$ for the primal variable is verified for all element geometries.

4. Numerical examples: convergence rates for regular meshes

Results are presented for simulations based on affine meshes in order to illustrate optimal convergence rates achieved for the three kinds of space configurations described in the previous section, in L^2 -norms of primal and dual errors. Errors in L^2 -norm for the divergence of the flux have been computed (not shown), and the obtained convergence rates coincide with the optimal ones of the pressure variable, as expected for the used space configurations based on affine meshes verifying exactly the property (1).

The test problem is defined in $\Omega = (0, 1)^3 \subset \mathbb{R}^3$ and has exact solution

$$u(x, y) = \sin \pi x \sin \pi y \sin \pi z. \quad (12)$$

For this problem, simulations are performed on regular meshes formed by tetrahedral, hexahedral, and prismatic elements. The hexahedral meshes are uniform with spacing 2^{-i} , $i = 0, 1, \dots, 4$. The tetrahedral meshes are obtained from the hexahedral ones by the subdivision of each cubic element into six tetrahedra. Similarly, the prismatic meshes are constructed by the subdivision of each hexahedral element into two prisms.

For comparison, similar results are shown for simulations based on the classical H^1 -conforming formulation: find $u \in H_0^1(\Omega)$

$$\int_{\Omega} \nabla u \cdot \nabla \varphi \, d\Omega = \int_{\Omega} f \varphi \, d\Omega, \quad \forall \varphi \in H_0^1(\Omega).$$

For this H^1 -conforming formulation, continuous approximation spaces of P_k type are applied, and static condensation can also be used by the organization of degrees of freedom of u in terms of internal, edge and vertex contributions, and by eliminating the internal contributions from the global matrix.

4.1. Results for tetrahedral elements

Fig. 1 presents the convergence curves in L^2 -norms versus h obtained with the mixed method using approximation spaces based on tetrahedral meshes. The errors in ∇u using the configurations $\mathbf{P}_k P_{k-1}$ (dotted lines), $\mathbf{P}_k^* P_k$ (continuous lines) and the $\mathbf{P}_k^{**} P_{k+1}$ (dashed lines) are displayed on the left side, in groups of different colours (magenta for $k = 1$, blue for $k = 2$, red for $k = 3$, and black for $k = 4$). The curves of each group have the same rate of decay $k + 1$, but the magnitudes occurring in the $\mathbf{P}_k P_{k-1}$ cases are significantly higher than in the other two configurations, which are quite similar. As expected, optimal convergence rates of orders k , $k + 1$, and $k + 2$ for the primal variable u are observed on the right side for $\mathbf{P}_k P_{k-1}$, $\mathbf{P}_k^* P_k$, and $\mathbf{P}_k^{**} P_{k+1}$ type of spaces, respectively.

Using static condensation, the number of equations to be solved with configurations $\mathbf{P}_k P_{k-1}$, $\mathbf{P}_k^* P_k$, and $\mathbf{P}_k^{**} P_{k+1}$ coincide, despite their differences in the total numbers of degrees of freedom. The plots in Fig. 2 are for the case $k = 3$, and the errors for the $\mathbf{P}_3 P_2$, $\mathbf{P}_3^* P_3$, and $\mathbf{P}_3^{**} P_4$ cases are considered in terms of the number of equations to be solved. Having the same number of degrees of freedom in the static condensed form, these plots illustrate the significant enhancement of pressure resolution when the $\mathbf{P}_3^* P_3$ or $\mathbf{P}_3^{**} P_4$ configurations are employed instead of the $\mathbf{P}_3 P_2$ setting. As expected, order rate 4 of flux accuracy occurs for the three configurations, but flux error magnitudes for $\mathbf{P}_3^* P_3$, and $\mathbf{P}_3^{**} P_4$, which are quite similar, are smaller than in the $\mathbf{P}_3 P_2$ case. This figure also illustrates the gain in accuracy of the mixed formulation in the flux variable, when compared with the H^1 formulation using cubic polynomials.

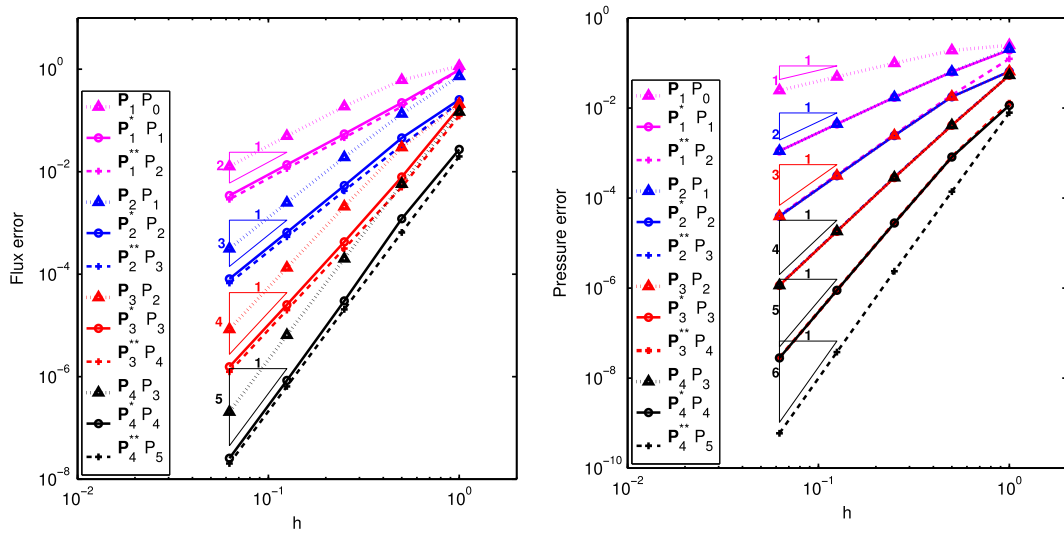


Fig. 1. 3D model problem using mixed formulation with tetrahedral elements: L^2 -errors for the flux ∇u (left side) and for the pressure u (right side) versus h , with spaces of type $\mathbf{P}_k - \mathbf{P}_{k-1}$ (dotted), $\mathbf{P}_k^* - \mathbf{P}_k$ (continuous), and $\mathbf{P}_k^{**} - \mathbf{P}_{k+1}$ (dashed), for $k = 1$ (magenta), $k = 2$ (blue), $k = 3$ (red), and $k = 4$ (black). (For interpretation of the references to colour in this figure legend, the reader is referred to the web version of this article.)

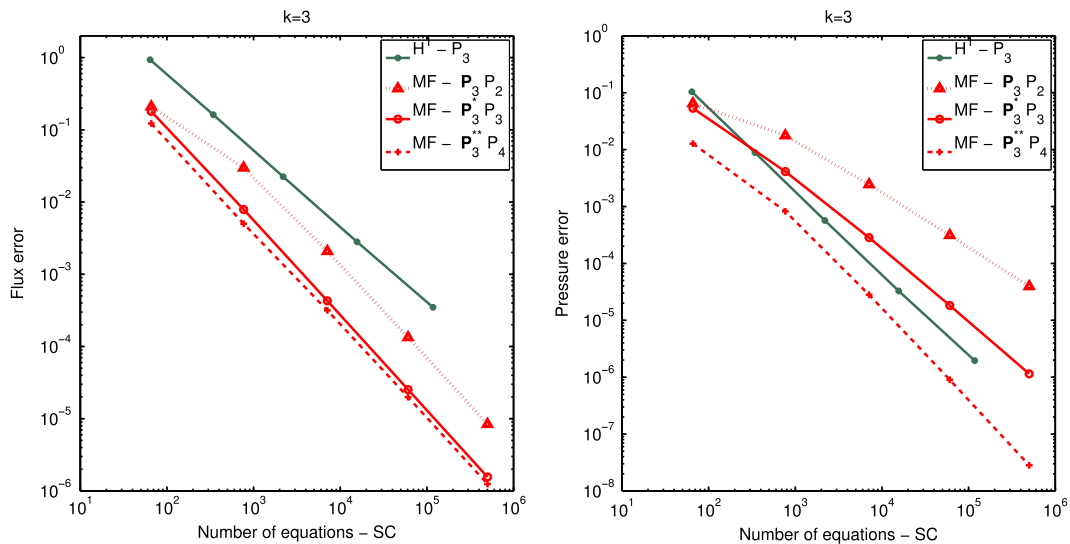


Fig. 2. 3D model problem with regular tetrahedral elements. Flux error (left) and pressure error (right) versus number of equations in the static condensed form: using mixed formulation with spaces of type $\mathbf{P}_3 - \mathbf{P}_2$ (dotted), $\mathbf{P}_3^* - \mathbf{P}_3$ (continuous), and $\mathbf{P}_3^{**} - \mathbf{P}_4$ (dashed), and H^1 formulation with spaces of type \mathbf{P}_3 (green). (For interpretation of the references to colour in this figure legend, the reader is referred to the web version of this article.)

In Fig. 3 the plots are for the mixed formulation with space configurations $\mathbf{P}_4^* - \mathbf{P}_4$ and $\mathbf{P}_4^{**} - \mathbf{P}_5$. The errors are considered in terms of the number of solved equations, with or without using static condensation, demonstrating the significant impact in the reduction of degrees of freedom when static condensation is applied. For comparison, the results for the H^1 formulation based on spaces of type \mathbf{P}_4 are also included, for which the effect of static condensation is not as significant as in the mixed formulation cases. As observed in the plots of the errors in terms of mesh spacing h of Fig. 1, for configurations having the same order in the primal variable, the corresponding pressure errors curves are quite indistinguishable. In Fig. 4 the cases $\mathbf{P}_4 - \mathbf{P}_3$, $\mathbf{P}_3^* - \mathbf{P}_3$, and $\mathbf{P}_2^{**} - \mathbf{P}_3$ are illustrated, where the errors are plotted in terms of the number of equations to be solved in the static condensation procedure. There, with almost identical error magnitudes, the pressure error curves are separated due to the difference in degrees of freedom required by the

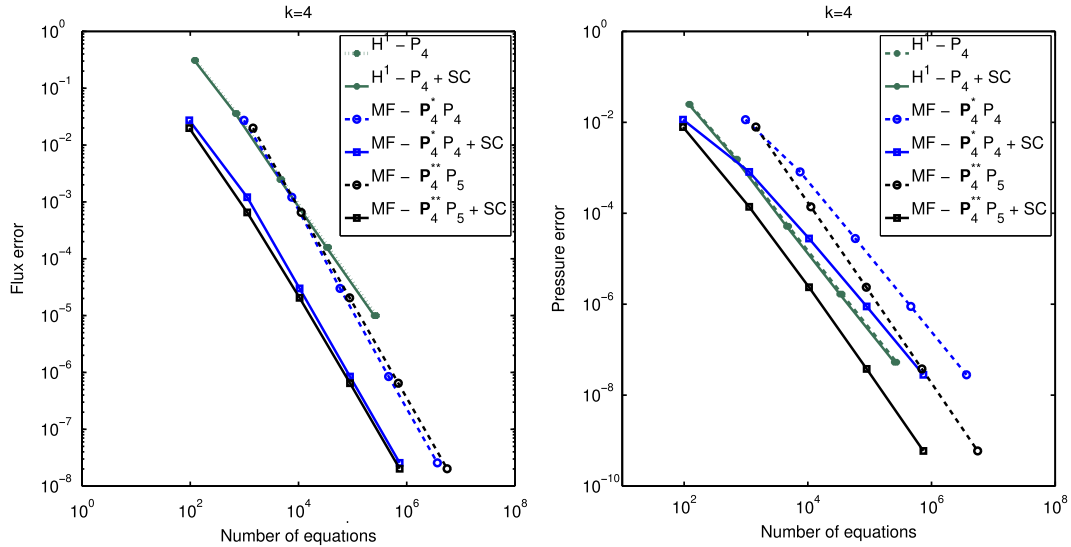


Fig. 3. 3D model problem with tetrahedral elements: L^2 -errors for the flux (left) and pressure (right) versus number of equations, using static condensation (continuous) or not (dotted): mixed formulation with spaces of type $\mathbf{P}_4^* P_4$ (blue), $\mathbf{P}_4^{**} P_5$ (black), and H^1 formulation with spaces of type P_4 (green). (For interpretation of the references to colour in this figure legend, the reader is referred to the web version of this article.)

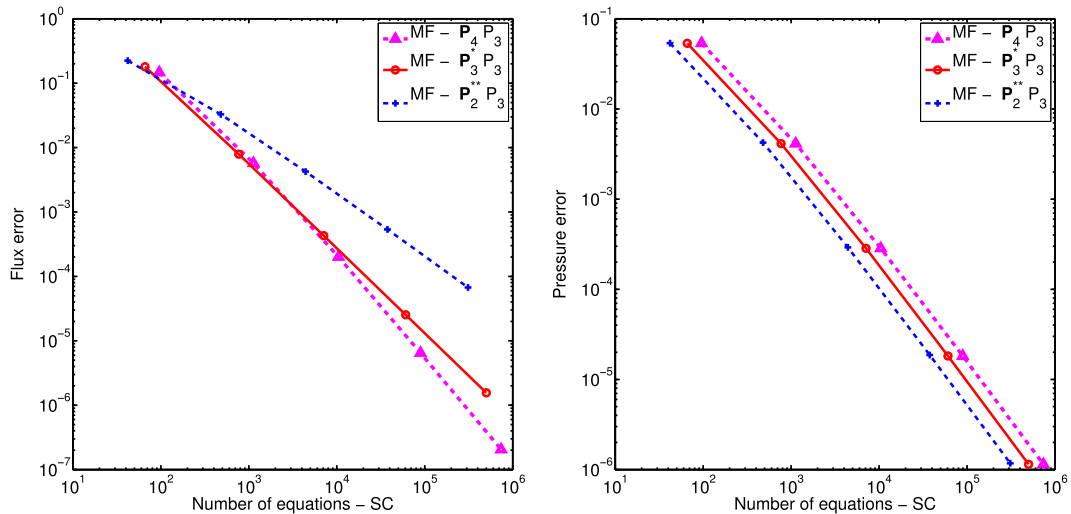


Fig. 4. 3D model problem with regular tetrahedral elements: L^2 -errors for the flux (left) and pressure (right) versus number of equations in the static condensed form: using mixed formulation with spaces of type $\mathbf{P}_4 P_3$ (dotted), $\mathbf{P}_3^* P_3$ (continuous), and $\mathbf{P}_2^{**} P_3$ (dashed).

different settings. The effect in the decay in flux accuracy can be also observed from the configuration $\mathbf{P}_4 P_3$ to the other two ones, where the $\mathbf{H}(\text{div})$ -approximation spaces are such that $\mathbf{P}_2^{**} \subset \mathbf{P}_3^* \subset \mathbf{P}_4$.

The plots on the left side of Fig. 5 compare the number of degrees of freedom DoF , as a function of the characteristic lengths h of the meshes, occurring on the discrete mixed formulations based on approximation spaces of type $\mathbf{P}_k^* P_k$ (left side) and $\mathbf{P}_k^{**} P_{k+1}$ (right side), with static condensation (dashed lines) and without static condensation (continuous lines).

In both cases, DoF increases at a cubic rate as the meshes are refined. Observe the drastic DoF reduction when static condensation is applied. For instance, the combination of spaces $\mathbf{P}_3^* P_3$ with static condensation, which gives convergence rates of order 4 for dual and primal variables, requires about the same number of equations to be solved as the lowest second order $\mathbf{P}_1^* P_1$ setting without using static condensation. This comparison is even more significant for the spaces $\mathbf{P}_4^{**} P_5$ with static condensation, which gives convergence rates of order 5 for the dual variable and 6

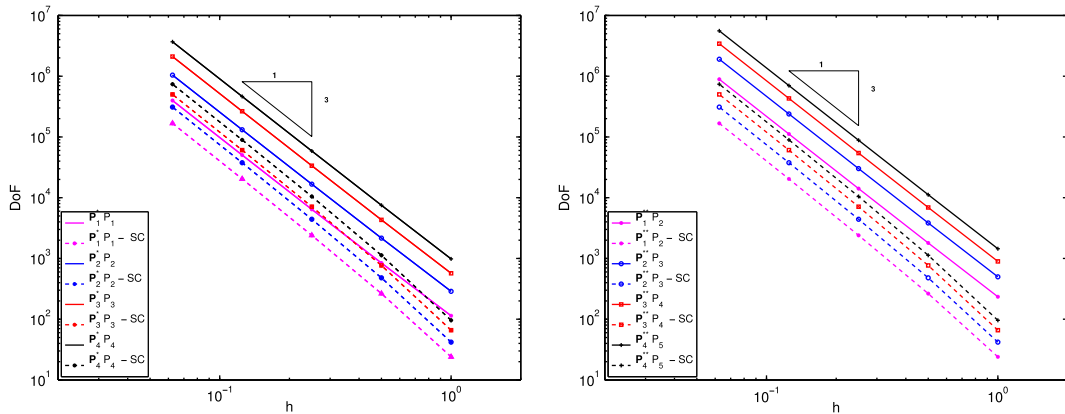


Fig. 5. 3D test problem using tetrahedra: number of equations to be solved in the mixed formulation with approximation spaces of type $\mathbf{P}_k^* P_k$ (left), and $\mathbf{P}_k^* P_{k+1}$ (right), with static condensation (dashed lines) and without static condensation (continuous lines), for $k = 1, 2, 3$, and 4 .

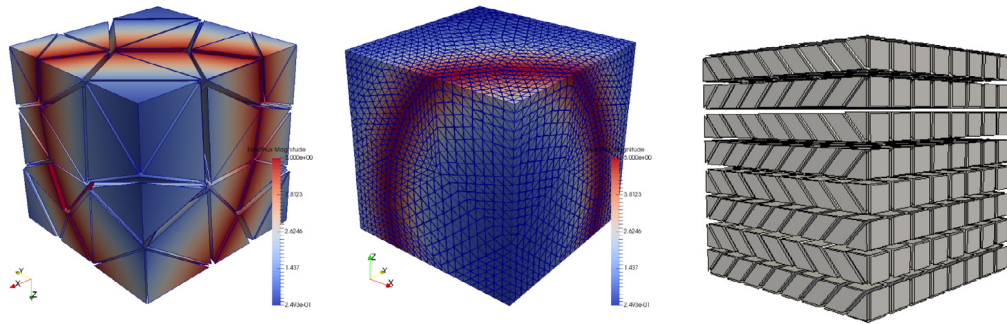


Fig. 6. Perspective views of irregular affine meshes with tetrahedral elements (left and middle sides) and hexahedral elements in a zig-zag pattern (right side).

for the primal variable, requiring less equations to be solved than the lowest second order $\mathbf{P}_1^* P_1$ setting without using static condensation.

4.2. Results for hexahedral and prismatic elements

Tables 2 and 3 present h -convergence histories for dual and primal variables obtained with approximation spaces of $\mathbf{P}_k^* P_k$, and $\mathbf{P}_k^* P_{k+1}$ types for hexahedral and prismatic geometries, respectively. All the conclusions derived for these configurations in the tetrahedral case are also satisfied for the hexahedral and prismatic geometries.

5. Robustness in the presence of irregular affine meshes

In order to confirm that the higher convergence rates observed in the previous simulations do not come from a super-convergence effect due to mesh regularity, we have constructed two families of irregular affine meshes. For the first example, a coarse irregular affine tetrahedral mesh for the unitary cubic region is constructed by a mesh generator. Then, three steps of subdivisions are applied to generate a sequence of irregular tetrahedral meshes. A second example considers a sequence of four hexahedral meshes which are generated by extruding two dimensional zig-zag meshes in the z -direction. These meshes are completed with some prisms in order to fill the unitary cubic region. Note that they are not obtained by successive refinements of a coarse mesh, but their elements are still affine. Perspective views of these kinds of meshes are shown in Fig. 6.

For the tests using tetrahedral meshes, the boundary value problem has exact solution $u = \frac{\pi}{2} - \text{atan}\left[5\left(\sqrt{(x-1.25)^2 + (y+0.25)^2 + (z+0.25)^2} - \frac{\pi}{3}\right)\right]$, and the formulation is set with Dirichlet boundary condition, accordingly. Fig. 7 presents the convergence curves in L^2 -norms for the flux ∇u (left side) and for u

Table 2

3D model problem: L^2 -errors and convergence rates using mixed formulation with spaces of type $\mathbf{P}_k^* P_k$ and $\mathbf{P}_k^{**} P_{k+1}$ based on uniform hexahedral elements.

Hexahedral meshes								
Spaces	$\mathbf{P}_1^* P_1$				$\mathbf{P}_1^{**} P_2$			
h	Pressure		Flux		Pressure		Flux	
	Error	Rate	Error	Rate	Error	Rate	Error	Rate
1	2.46E−01		1.17E00		1.54E−01		1.06E00	
2^{-1}	5.42E−02	2.18	2.44E−01	2.27	1.11E−02	3.79	1.49E−01	2.83
2^{-2}	1.40E−02	1.96	6.22E−02	1.97	1.30E−03	3.09	3.62E−02	2.04
2^{-3}	3.51E−03	1.99	1.56E−02	1.99	1.60E−04	3.02	8.97E−03	2.01
2^{-4}	8.79E−04	2.00	3.91E−03	2.00	2.00E−05	3.01	2.24E−03	2.00
Spaces	$\mathbf{P}_2^* P_2$				$\mathbf{P}_2^{**} P_3$			
h	Pressure		Flux		Pressure		Flux	
	Error	Rate	Error	Rate	Error	Rate	Error	Rate
1	1.50E−02		6.74E−02		1.50E−02		6.74E−02	
2^{-1}	7.26E−03	1.04	3.25E−02	1.05	9.16E−04	4.03	1.56E−02	2.11
2^{-2}	9.28E−04	2.97	4.13E−03	2.98	6.10E−05	3.91	2.04E−03	2.94
2^{-3}	1.17E−04	3.99	5.18E−04	2.99	3.88E−06	3.97	2.58E−04	2.98
2^{-4}	1.46E−05	4.00	6.48E−05	3.00	2.44E−07	3.99	3.24E−05	3.00
Spaces	$\mathbf{P}_3^* P_3$				$\mathbf{P}_3^{**} P_4$			
h	Pressure		Flux		Pressure		Flux	
	Error	Rate	Error	Rate	Error	Rate	Error	Rate
1	1.50E−02		6.74E−02		2.35E−03		3.92E−02	
2^{-1}	7.23E−04	4.37	3.48E−03	4.28	6.73E−05	5.12	1.32E−03	4.89
2^{-2}	4.59E−05	3.98	2.04E−04	4.09	2.09E−06	5.01	8.07E−05	4.03
2^{-3}	2.89E−06	3.99	1.28E−05	3.99	6.52E−08	5.00	5.02E−06	4.01
2^{-4}	1.81E−07	4.00	8.02E−07	4.00	2.04E−09	5.00	3.13E−07	4.00
Spaces	$\mathbf{P}_4^* P_4$				$\mathbf{P}_4^{**} P_5$			
h	Pressure		Flux		Pressure		Flux	
	Error	Rate	Error	Rate	Error	Rate	Error	Rate
1	3.20E−04		1.43E−03		3.20E−04		1.43E−03	
2^{-1}	5.72E−05	2.48	2.94E−04	2.28	4.25E−06	6.23	9.19E−05	3.96
2^{-2}	1.81E−06	4.98	8.07E−06	5.19	6.83E−08	5.96	2.93E−06	4.97
2^{-3}	5.69E−08	4.99	2.53E−07	4.99	1.08E−09	5.99	9.23E−08	4.99
2^{-4}	1.78E−09	5.00	7.91E−09	5.00	1.69E−11	6.00	2.89E−09	5.00

(right side) variables based on the irregular family of tetrahedral meshes, and using the configurations $\mathbf{P}_2 P_1$ (dotted lines), $\mathbf{P}_2^* P_2$ (continuous lines) and the $\mathbf{P}_2^{**} P_3$ (dashed lines). It can be observed that, for this kind of irregular affine meshes, the obtained rates of convergence are in agreement with the a priori predicted ones.

For the simulations based on zig-zag hexahedral meshes, the test problem is the one considered in the previous section, with exact solution defined in (12). Tables 4 and 5 show the errors in u and ∇u of the simulations with space configurations of type $\mathbf{P}_k^* P_k$ and $\mathbf{P}_k^{**} P_{k+1}$. Again, the same convergence rates are obtained as when using uniform hexahedral meshes, demonstrating the robustness of the proposed schemes for the mixed formulation of the Poisson problem. Table 6 presents divergence error in L^2 -norm, confirming the optimal rates expected for these affine meshes.

6. Conclusions

Different choices of balanced finite element approximation spaces for dual and primal variables, based on tetrahedral, hexahedral and prismatic meshes, are considered and compared for discrete versions of the mixed finite element method for three dimensional elliptic problems. The shape functions are constructed from polynomials of

Table 3

3D model problem: L^2 -errors errors and convergence rates using mixed formulation with spaces of type $\mathbf{P}_k^* P_k$ and $\mathbf{P}_k^{**} P_{k+1}$ based on uniform prismatic elements.

Prismatic meshes

Spaces h	$\mathbf{P}_1^* P_1$				$\mathbf{P}_1^{**} P_2$			
	Pressure		Flux		Pressure		Flux	
	Error	Rate	Error	Rate	Error	Rate	Error	Rate
1	2.27E−01		1.10E00		1.43E−01		1.06E00	
2 ^{−1}	6.06E−02	1.90	2.44E−01	2.17	1.49E−02	3.26	1.67E−01	2.66
2 ^{−2}	1.60E−02	1.92	6.23E−02	1.97	1.88E−03	2.99	4.09E−02	2.03
2 ^{−3}	4.05E−03	1.98	1.57E−02	1.99	2.38E−04	2.99	1.01E−02	2.01
2 ^{−4}	1.01E−03	2.00	3.92E−03	2.00	2.96E−05	3.00	2.53E−03	2.00
Spaces h	$\mathbf{P}_2^* P_2$				$\mathbf{P}_2^{**} P_3$			
	Pressure		Flux		Pressure		Flux	
	Error	Rate	Error	Rate	Error	Rate	Error	Rate
1	4.81E−02		1.82E−01		3.50E−02		1.42E−01	
2 ^{−1}	1.23E−02	1.97	4.39E−02	2.05	2.22E−03	3.98	2.28E−02	2.64
2 ^{−2}	1.62E−03	2.92	5.61E−03	2.97	1.47E−04	3.92	2.92E−03	2.97
2 ^{−3}	2.06E−04	2.98	7.06E−04	2.99	9.28E−06	3.98	3.67E−04	2.99
2 ^{−4}	2.58E−05	2.99	8.83E−05	3.00	5.82E−07	4.99	4.59E−05	3.00
Spaces h	$\mathbf{P}_3^* P_3$				$\mathbf{P}_3^{**} P_4$			
	Pressure		Flux		Pressure		Flux	
	Error	Rate	Error	Rate	Error	Rate	Error	Rate
1	3.48E−02		1.31E−01		5.52E−03		6.98E−02	
2 ^{−1}	2.07E−03	4.07	6.95E−03	4.24	3.10E−04	4.15	3.05E−03	4.51
2 ^{−2}	1.36E−04	3.92	4.45E−04	3.96	1.01E−05	4.94	1.91E−04	4.00
2 ^{−3}	8.65E−06	3.98	2.80E−05	3.99	3.18E−07	4.99	1.19E−05	4.01
2 ^{−4}	5.42E−07	4.00	1.75E−06	4.00	9.95E−09	5.00	7.43E−07	4.00
Spaces h	$\mathbf{P}_4^* P_4$				$\mathbf{P}_4^{**} P_5$			
	Pressure		Flux		Pressure		Flux	
	Error	Rate	Error	Rate	Error	Rate	Error	Rate
1	3.79E−03		2.02E−02		2.59E−03		9.66E−03	
2 ^{−1}	2.94E−04	3.69	9.63E−04	4.40	3.86E−05	6.07	3.96E−04	4.60
2 ^{−2}	9.67E−06	4.93	3.09E−05	4.96	6.15E−07	5.97	1.21E−05	5.02
2 ^{−3}	3.06E−07	4.98	9.71E−07	5.00	9.64E−09	6.00	3.76E−07	5.01
2 ^{−4}	9.60E−09	5.00	3.04E−08	5.00	1.51E−10	6.00	1.17E−08	5.00

total degree k for tetrahedra, of maximum degree k for hexahedra, and of total degree k in the triangular faces of prismatic elements, and with maximum degree k in the complementary direction.

For tetrahedral meshes, there is the combination of spaces of type $\mathbf{P}_k P_{k-1}$. Other configurations denoted by $\mathbf{P}_k^* P_k$ and $\mathbf{P}_k^{**} P_{k+1}$ are analysed for all geometries, where \mathbf{P}_k^* and \mathbf{P}_k^{**} are obtained by enriching the complete flux space of type \mathbf{P}_k with some internal flux functions with degree up to $k + 1$ or $k + 2$, respectively.

In fact, the space configurations $\mathbf{P}_k P_{k-1}$ and $\mathbf{P}_k^* P_k$ are connected to other classic families of spaces, as summarized in Table 7. The idea of enhancing the primal variable accuracy by increasing the order of the internal flux functions in the innovative $\mathbf{P}_k^{**} P_{k+1}$ configuration was motivated by recent similar results in the context of the Multiscale Hybrid Method in [19], where refined H^1 approximations are applied inside the macro elements.

In order to compare the performance of the three kinds of space configurations, convergence studies are presented using families of hierarchical shape functions specially designed for affine meshes. As expected, optimal rates in L^2 -norms for primal and dual variables are observed, which are determined by the degree of the complete polynomial spaces included in the corresponding approximations spaces. In fact, the convergence rates of order $k + 1$ for the dual variable do not change by increasing the degrees of internal flux functions, as documented in \mathbf{P}_k^* and \mathbf{P}_k^{**} . But

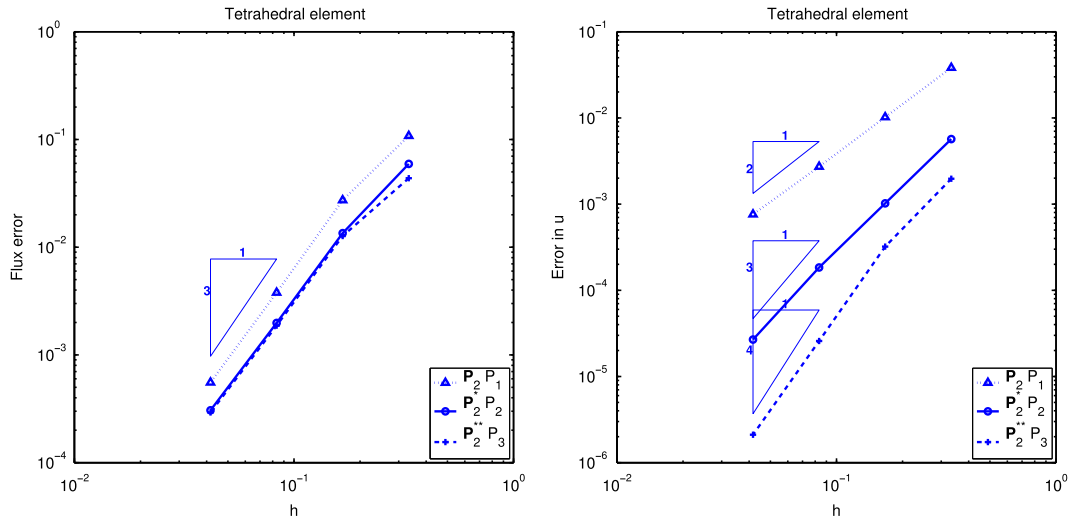


Fig. 7. 3D model problem using mixed formulation with irregular affine tetrahedral meshes: L^2 -errors for the flux (left side) and pressure (right side) versus h , with spaces of type $\mathbf{P}_2^* P_1$ (dotted), $\mathbf{P}_2^* P_2$ (continuous), and $\mathbf{P}_2^{**} P_3$ (dashed).

Table 4

L^2 -errors in u and rates of convergence for the model problems using mixed formulation and spaces of type $\mathbf{P}_k^* P_k$ and $\mathbf{P}_k^{**} P_{k+1}$ based on zig-zag hexahedral meshes.

L^2 -errors in u using zig-zag hexahedral meshes

Spaces	$\mathbf{P}_1^* P_1$		$\mathbf{P}_2^* P_2$		$\mathbf{P}_3^* P_3$		$\mathbf{P}_4^* P_4$	
Level	Error	Rate	Error	Rate	Error	Rate	Error	Rate
1	7.93E-02		1.80E-02		3.45E-03		5.37E-04	
2	2.33E-02	1.77	2.76E-03	2.70	2.66E-04	3.69	2.08E-05	4.69
3	6.17E-03	1.92	3.72E-04	2.89	1.80E-05	3.89	7.03E-07	4.89
4	1.58E-03	1.97	4.79E-05	2.96	1.16E-06	3.95	2.27E-08	4.95

Spaces	$\mathbf{P}_1^{**} P_2$		$\mathbf{P}_2^{**} P_3$		$\mathbf{P}_3^{**} P_4$		$\mathbf{P}_4^{**} P_5$	
Level	Error	Rate	Error	Rate	Error	Rate	Error	Rate
1	2.09E-02		3.63E-03		5.57E-04		7.24E-05	
2	3.04E-03	2.78	2.81E-04	3.70	2.15E-05	4.69	1.40E-06	5.69
3	4.03E-04	2.91	1.90E-05	3.89	7.25E-07	4.90	2.36E-08	5.89
4	5.17E-05	2.96	1.22E-06	3.95	2.34E-08	4.95	3.82E-10	5.95

higher optimal convergence rates (i.e. $k + 1$ and $k + 2$) are obtained for the pressure variable when using the $\mathbf{P}_k^* P_k$ and $\mathbf{P}_k^{**} P_{k+1}$ function spaces, respectively, which are higher than the order k obtained when using the $\mathbf{P}_k P_{k-1}$ configuration. These results are summarized in Table 8, including the optimal convergence rates for the divergence of the flux.

In all three settings, the degrees of freedom associated with internal flux functions can be condensed. Therefore, for each element geometry, and fixed degree k used in the border flux approximations, the resulting global matrices have identical sizes. The effect of static condensation is analysed in terms of the size reduction of the global system to be solved. For high order approximations, the number of condensed equations amounts to more than 80% of the total number of equations, which demonstrates the potential benefit of using $\mathbf{H}(\text{div})$ approximation spaces in parallel computers. The $\mathbf{H}(\text{div})$ approximations with increased internal order are more precise than the H^1 approximations as a function of mesh size and number of condensed equations. Currently, the authors are engaged in the extension of the proposed methodology to treat more general geometries, combined with Piola pullback map of the vector fields. Preliminary results are reported in [26] for $\mathbf{P}_k^* P_k$ space configurations based on curved triangular or quadrilateral meshes on the plane or on manifolds immersed in \mathbb{R}^3 .

Table 5

L^2 -errors in ∇u and rates of convergence for the model problems using mixed formulation and spaces of type $\mathbf{P}_k^* P_k$ and $\mathbf{P}_k^{**} P_{k+1}$ based on zig-zag hexahedral meshes.

L^2 -errors in $\sigma = \nabla u$ using zig-zag hexahedral meshes

Spaces	$\mathbf{P}_1^* P_1$		$\mathbf{P}_2^* P_2$		$\mathbf{P}_3^* P_3$		$\mathbf{P}_4^* P_4$	
Level	Error	Rate	Error	Rate	Error	Rate	Error	Rate
1	3.24E-01		6.27E-02		1.15E-03		1.75E-03	
2	8.75E-02	1.89	9.19E-03	2.77	8.58E-04	3.75	6.60E-05	4.72
3	2.24E-02	1.96	1.22E-03	2.91	5.73E-05	3.91	2.22E-06	4.90
4	5.67E-03	1.98	1.57E-04	2.96	3.68E-06	3.96	7.15E-08	4.95
Spaces	$\mathbf{P}_1^{**} P_2$		$\mathbf{P}_2^{**} P_3$		$\mathbf{P}_3^{**} P_4$		$\mathbf{P}_4^{**} P_5$	
Level	Error	Rate	Error	Rate	Error	Rate	Error	Rate
1	2.00E-01		3.14E-02		4.94E-03		6.71E-04	
2	5.08E-02	1.98	4.51E-03	2.80	3.59E-04	3.78	2.49E-05	4.75
3	1.28E-02	1.99	5.98E-04	2.92	2.38E-05	3.92	8.34E-07	4.90
4	3.20E-03	2.00	7.66E-05	2.96	1.53E-06	3.96	2.69E-08	4.96

Table 6

L^2 -errors in $\nabla \cdot \sigma$ and rates of convergence for the model problems using mixed formulation and spaces of type $\mathbf{P}_k^* P_k$ and $\mathbf{P}_k^{**} P_{k+1}$ based on zig-zag hexahedral meshes.

L^2 -errors in $\nabla \cdot \sigma$ using zig-zag hexahedral meshes

Spaces	$\mathbf{P}_1^* P_1$		$\mathbf{P}_2^* P_2$		$\mathbf{P}_3^* P_3$		$\mathbf{P}_4^* P_4$	
Level	Error	Rate	Error	Rate	Error	Rate	Error	Rate
1	2.33E00		5.31E-01		1.02E-01		1.59E-02	
2	6.89E-01	1.76	8.17E-02	2.70	7.89E-03	3.70	6.16E-04	4.69
3	1.83E-01	1.92	1.10E-02	2.89	5.32E-04	3.89	2.08E-05	4.89
4	4.67E-02	1.97	1.42E-03	2.95	3.43E-05	3.96	6.72E-07	4.95
Spaces	$\mathbf{P}_1^{**} P_2$		$\mathbf{P}_2^{**} P_3$		$\mathbf{P}_3^{**} P_4$		$\mathbf{P}_4^{**} P_5$	
Level	Error	Rate	Error	Rate	Error	Rate	Error	Rate
1	5.31E-01		1.02E-01		1.59E-02		2.08E-03	
2	8.17E-02	2.70	7.89E-03	3.70	6.16E-04	4.69	4.04E-05	5.69
3	1.10E-02	2.89	5.32E-04	3.89	2.08E-05	4.89	6.82E-07	5.89
4	1.42E-03	2.96	3.43E-05	3.96	6.72E-07	4.95	1.10E-08	5.95

Table 7

Connections with other classic spaces.

	$\mathbf{P}_k P_{k-1}$	$\mathbf{P}_k^* P_k$	$\mathbf{P}_k^{**} P_k$
\mathcal{T}_e	BDM_k	$BDFM_{k+1}$	New
\mathcal{H}	Unstable	RT_k	New
\mathcal{P}_r	Unstable	New	New

Table 8

Orders of convergence in L^2 -norms when spaces of type $\mathbf{P}_k P_{k-1}$, $\mathbf{P}_k^* P_k$ and $\mathbf{P}_k^{**} P_{k+1}$, based on affine elements, are applied to the mixed formulation.

Space configurations	Geometries	Order of convergence in L^2 -norms		
		u	$\sigma = \nabla u$	$\nabla \cdot \sigma$
$\mathbf{P}_k P_{k-1}$	\mathcal{T}_e	k	$k+1$	k
$\mathbf{P}_k^* P_k$	All	$k+1$	$k+1$	$k+1$
$\mathbf{P}_k^{**} P_{k+1}$	All	$k+2$	$k+1$	$k+2$

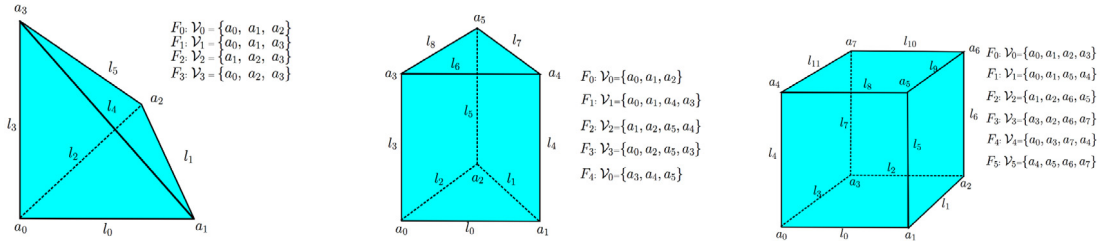


Fig. A.8. Basic geometric elements of the tetrahedron (left side), prism (middle side) and hexahedron (right side).

Acknowledgements

The authors P.R.B. Devloo, and S.M. Gomes thankfully acknowledge financial support from ANP-Brazilian National Agency of Petroleum, Natural Gas and Biofuels (grant SAP4600333146), and from CNPq, the Brazilian Research Council (grants 310369/2006-1 and 308632/2006-0). D.A. Castro is grateful for the hospitality received during his pos-doc visit at LabMeC-FEC-Unicamp, when this paper was prepared, and for financial support received from FAPESP-Research Foundation of the State of São Paulo, Brazil (grant 2013/21959-4). A.M. Farias thankfully acknowledges financial support from ANP (grant SAP4600333146) and from CAPES Foundation, within the Ministry of Education in Brazil (Grant PNPD/CAPES).

Appendix A. Construction of shape functions for approximation spaces in $\mathbf{H}(\text{div}, \Omega)$ for affine partitions

This section is dedicated to the description of a methodology for the construction of approximation subspaces $\mathbf{V}_k^\Gamma \subset \mathbf{H}(\text{div}, \Omega)$, based on a partition $\Gamma = \{K\}$ of Ω . It is satisfied for arbitrary meshes formed by affine elements of triangular or rectangular geometric types in 2D, and tetrahedral, cubic or prismatic geometric types in 3D. Since the two-dimensional geometries have already been discussed in [20], a detailed explanation is given for the 3D case only. The description here applies to regular partitions, without hanging sides, and uniform distribution of polynomial degrees. Extensions to irregular *hp*-meshes are also possible, as described in [21] for two-dimensional quadrilateral and triangular cases.

A.1. Hierarchical scalar bases

For regular geometric partitions (no hanging sides), the construction of scalar continuous finite element approximation subspaces used in NeopZ is documented in [24]. Here, we recall some of their specific aspects that are useful for the current purposes.

Concepts regarding geometry

We shall assume that there is an affine transformation $\mathbf{x} : \mathbb{R}^3 \rightarrow \mathbb{R}^3$ mapping a master element \hat{K} onto K . Namely, the tetrahedron, hexahedron and prism master elements are, respectively, $\hat{K} = \mathcal{T}e$, $\hat{K} = \mathcal{H}$ and $\hat{K} = \mathcal{P}r$ defined by

$$\begin{aligned} \mathcal{T}e &= \{\xi = (\xi_0, \xi_1, \xi_2); \xi_0 \geq 0, \xi_1 \geq 0, \xi_2 \geq 0, \xi_0 + \xi_1 + \xi_2 \leq 1\}, \\ \mathcal{H} &= [-1, 1]^3, \quad \mathcal{P}r = \mathcal{T} \times [0, 1] \end{aligned}$$

where $\mathcal{T} = \{\xi = (\xi_0, \xi_1); \xi_0 \geq 0, \xi_1 \geq 0, \xi_0 + \xi_1 \leq 1\}$ is the triangular reference element.

Given an element $K \subset \mathbb{R}^3$, let \mathcal{V} , \mathcal{E} and \mathcal{F} be the sets of the vertices, edges and faces of K , respectively. The basic geometric elements of K are indicated in Fig. A.8, and the corresponding ones in the geometric element K are mapped from \hat{K} by the geometric transformation \mathbf{x} . For each face $F \in \mathcal{F}$, let \mathcal{V}_F and \mathcal{E}_F be the sets of vertices and edges of F . Given a vertex $a \in \mathcal{V}$, define \mathcal{F}_a as the set of the faces sharing a . Similarly, \mathcal{F}_l is the set of the faces sharing the edge l . One edge is said to be adjacent to the face F by the vertex $a \in \mathcal{V}_F$ if it is common to the two incident faces over F that share this vertex. Similarly, given an edge $l \in \mathcal{E}_F$, the face sharing l with F is called adjacent to F by this edge.

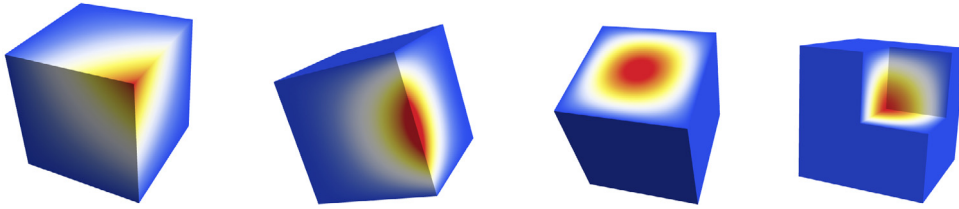


Fig. A.9. Scalar shape functions of vertex type (left side), edge and face type (middle side), and internal type (right side).

Table A.9

Number of scalar shape functions in \mathbf{B}_k^K .

	Vertex	Edge	Face	Internal	Total
$\mathcal{T}e$	4	$6(k-1)$	$\frac{1}{2}(k-1)(k-2)$	$\frac{1}{6}(k-1)(k-2)(k-3)$	$\frac{1}{6}(k+1)(k+2)(k+3)$
\mathcal{H}	8	$12(k-1)$	$6(k-1)^2$	$(k-1)^3$	$(k+1)^3$
$\mathcal{P}r$	6	$9(k-1)$	$(k-1)(4k-5)$	$\frac{1}{2}(k-1)^2(k-2)$	$\frac{1}{2}(k+1)^2(k+2)$

Scalar shape functions

The scalar shape functions considered in the present paper are described in [24]. They are defined on the master element and then transformed to the computational element K by the geometric transformation, and form hierarchical bases \mathcal{B}_k^K for subspaces of $H^1(K)$. The index k refers to the degree of polynomial spaces P_k spanned by them on the master element. For tetrahedra, the polynomials in P_k have total degree k , for hexahedra, they have maximum degree k in each coordinate, and for prismatic elements, P_k is formed by polynomials of total degree k in the (ξ_0, ξ_1) , and of maximum degree k in ξ_2 .

Each shape function is associated with one of the basic elements of K , namely, vertex, edge, face or the volume K itself, which are characterized by the following main properties:

- Vertex functions $\varphi^a(\xi)$: they are traditional Lagrangian first order basis functions such $\varphi^a(a) = 1$, and vanish in all vertices different from a , and faces not sharing the vertex a .
- Edge functions $\varphi^{l,n}(\xi)$: they vanish in all edges different from l , and in all faces not sharing l .
- Face functions $\varphi^{F,n_1,n_2}(\xi)$, they vanish in all edges, vertices, and faces other than F .
- Internal functions $\varphi^{K,n_1,n_2,n_3}(\xi)$: they vanish in all faces, edges and vertices of K .

The shape functions associated with edge, face and volume elements are formed by the product of two functions. The first one, called blending function, is a specific combination of vertex functions. There is one blending function for each basic element, and its role is to enforce the corresponding vanishing property on the other elements. In order to increase the degrees of the shape functions, the blending functions are multiplied by a product of Chebyshev polynomials (of degree n or n_i), which vary according to particular geometry. These Chebyshev polynomials are evaluated in parameters determined by appropriate affine transformations of the master element coordinates. There is one affine transformation for each basic element.

The resulting set of functions

$$\mathcal{B}_k^K = \left\{ \varphi^{a_m}, \varphi^{l_m,n}, \varphi^{F_m,n_1,n_2}, \varphi^{K,n_1,n_2,n_3} \right\}$$

is linearly independent, spanning a subspace of $H^1(K)$. The total numbers of each type of shape functions in \mathcal{B}_k^K are indicated in Table A.9. Illustrations of some vertex, edge, face and internal functions are shown in Fig. A.9.

Continuous assemblage of scalar functions

Let K^ℓ and K^j be neighbour elements sharing a face $F = K^\ell \cap K^j$. It is clear that the traces on F of corresponding vertex shape functions in K^ℓ and K^j , associated with a vertex of F , coincide. The appropriate choice of the parametric affine transformations of the master element used in the definition of the corresponding edge and face functions on both sides, associated with F , also make these shape functions continuous across this interface. Consequently, if u is a scalar piecewise function defined by $u|_K = u_K \in \text{span } \mathcal{B}_k^K$ on the elements of Γ , then the continuity of u is

obtained by requiring equality of multiplying coefficients of vertex, edge or face functions of the expansions of u_{K^ℓ} and u_{K^j} . Internal shape functions, edge and face functions not interacting with F do not contribute to this continuous assemblage, since they vanish on this interface.

A.2. Vector fields

Connected to each basic geometric element of K (vertex, edge, face, or volume), three linearly independent constant vector fields are defined by the following instructions:

- For each vertex $a \in \mathcal{V}$, there are three fields $\mathbf{v} = \mathbf{v}^{F,a}$, each one associated with a face $F \in \mathcal{F}_a$ having a as one of its vertices. The vector $\mathbf{v}^{F,a}$ should be aligned to the edge adjacent to F by the vertex a . Furthermore, it is normalized to have unit normal component over F .
- For each edge $l \in \mathcal{E}$, there is a vector $\mathbf{v} = \mathbf{v}^{l,\top}$, aligned to l , and there are two vectors $\mathbf{v} = \mathbf{v}^{F,l}$, which are incident to $F \in \mathcal{F}_l$ and parallel to the face adjacent to F by l . They are normalized to have unit normal component over F .
- For each face F , there is the outward unit normal $\mathbf{v} = \mathbf{v}^{F,\perp}$ and two linearly independent vectors $\mathbf{v} = \mathbf{v}_{(j)}^{F,\top}$, $j = 1, 2$ tangent to F .
- Associated with the volume K itself, there are orthonormal vector fields $\mathbf{v} = \mathbf{v}_{(j)}^K = \mathbf{e}_{(j)}$, $j = 1, 2, 3$ associated with it. For instance, they can be defined by the canonical orthonormal vectors $e_{(1)} = (1, 0, 0)$, $e_{(2)} = (0, 1, 0)$ and $e_{(3)} = (0, 0, 1)$.

The vector fields are grouped into two categories:

1. Face vector fields, which are incident to the faces $F \in \mathcal{F}$:
 - (a) $\mathbf{v} = \mathbf{v}^{F,a}$, vectors associated with the vertices $a \in \mathcal{V}_F$.
 - (b) $\mathbf{v} = \mathbf{v}^{F,l}$ vectors associated with the edges $l \in \mathcal{E}_F$.
 - (c) $\mathbf{v} = \mathbf{v}^{F,\perp}$ vector associated (normal) with the face F itself.
2. Internal vector fields
 - (a) $\mathbf{v} = \mathbf{v}^{l,\top}$, vector aligned to the edge $l \in \mathcal{E}$.
 - (b) $\mathbf{v} = \mathbf{v}_{(j)}^{F,\top}$, $j = 1, 2$, vectors tangent to the faces $F \in \mathcal{F}$.
 - (c) $\mathbf{v} = \mathbf{v}_{(j)}^K = \mathbf{e}_{(j)}$, $j = 1, 2$ and 3 , associated with the volume K .

On the top side of Fig. A.10, some face vector fields $\mathbf{v}^{F,a}$, $\mathbf{v}^{F,l}$ and $\mathbf{v}^{F,\perp}$ are illustrated: for the basic elements of the face $F = F_2$ of a tetrahedron (left side), and a hexahedron (right side), and of $F = F_1$ for a prismatic element (middle side). On the bottom side, some of the internal vector fields $\mathbf{v}^{l,\top}$, $\mathbf{v} = \mathbf{v}_{(j)}^{F,\top}$ are shown. Internal vector fields $\mathbf{v}_{(j)}^K$, which are the same for all elements, are not plotted.

A.3. Vectorial basis functions in $\mathbf{H}(\text{div}, K)$

Following the guideline presented in the beginning of the current section, the purpose is to construct vectorial bases \mathbf{B}_k^K formed by functions $\Phi \in \mathbf{H}(\text{div}, K)$ defined on the element K by the multiplication

$$\Phi = \varphi \mathbf{v},$$

where \mathbf{v} is one of the constant vector fields defined in Appendix A.2, and φ is one of the scalar basis functions in \mathcal{B}_k^K , described in Appendix A.1. It is clear that $\nabla \cdot \Phi = \mathbf{v} \cdot \nabla \varphi$, which implies that $\Phi \in \mathbf{H}(\text{div}, K)$. These vectorial shape functions shall be classified as face or internal functions.

Face functions:

- $\Phi^{F,a}$ - product of vertex scalar functions φ^a , associated with the vertices $a \in \mathcal{V}_F$, and the face vectors $\mathbf{v}^{F,a}$.
- $\Phi^{F,l,n}$ - product of the edge scalar functions $\varphi^{l,n}$, associated with the edges $l \in \mathcal{E}_F$, and face vectors $\mathbf{v}^{F,l}$.
- Φ^{F,n_1,n_2} - product of the face scalar functions φ^{F,n_1,n_2} , associated with the faces $F \in \mathcal{F}$, and the associated normal vectors $\mathbf{v}^{F,\perp}$.

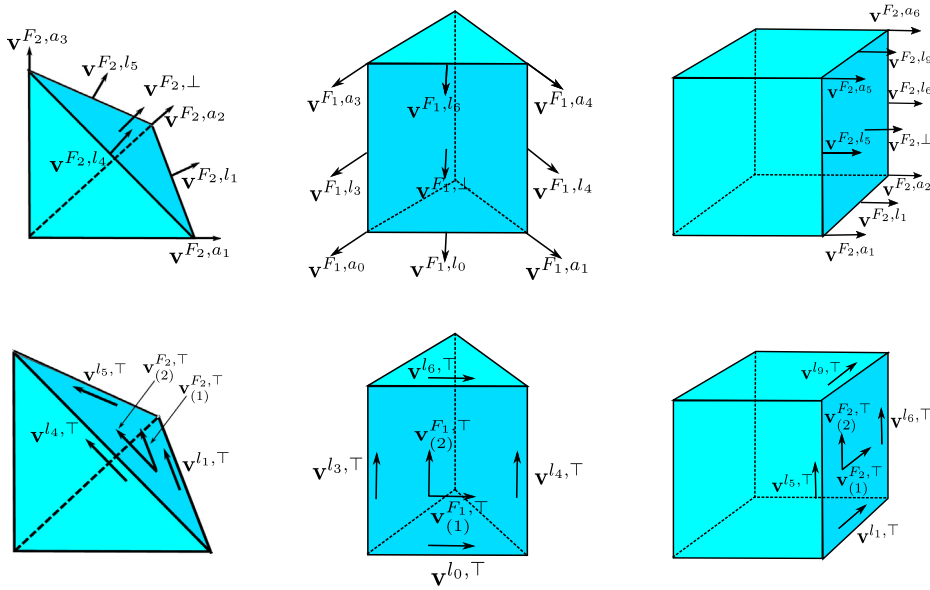


Fig. A.10. Illustration of face vector fields $\mathbf{v}^{F,a}$, $\mathbf{v}^{F,l}$ and $\mathbf{v}^{F,\perp}$ (top side) and internal vector fields $\mathbf{v}^{l,\top}$ and $\mathbf{v} = \mathbf{v}^{F,\top}_{(j)}$ (bottom side) associated to basic elements of a face F of a tetrahedron (left side), a prism (middle side), and a hexahedron (right side).

Internal functions:

- $\Phi^{K,l,n}$ - product of edge scalar functions $\varphi^{l,n}$ and vectors $\mathbf{v}^{l,\top}$ aligned to l .
- $\Phi^{K,F,n_1,n_2}_{(j)}$ - product of face scalar functions φ^{F,n_1,n_2} and vectors $\mathbf{v} = \mathbf{v}^{F,\top}_{(j)}$, $j = 1, 2$, tangent to F .
- $\Phi^{K,n_1,n_2,n_3}_{(j)}$ - product of internal scalar functions φ^{K,n_1,n_2,n_3} and three volume vector fields $\mathbf{v}^{K}_{(j)}$, $j = 1, 2$ and 3.

An illustration of the face function $\Phi^{F_0,a_1} = \varphi^{a_1} \mathbf{v}^{F_0,a_1}$ for a tetrahedron is given in Fig. A.11.

Let \mathbf{B}_k^K be the set formed by these face and internal vectorial shape functions

$$\mathbf{B}_k^K = \underbrace{\left\{ \Phi^{F,a}, \Phi^{F,l,n}, \Phi^{F,n_1,n_2} \right\}}_{\text{face functions}} \cup \underbrace{\left\{ \Phi^{K,l,n}, \Phi^{K,F,n_1,n_2}_{(1)}, \Phi^{K,F,n_1,n_2}_{(2)}, \Phi^{K,n_1,n_2,n_3}_{(1)}, \Phi^{K,n_1,n_2,n_3}_{(2)}, \Phi^{K,n_1,n_2,n_3}_{(3)} \right\}}_{\text{internal functions}}. \quad (\text{A.1})$$

It is clear that $\text{span } \mathbf{B}_k^K \subset \mathbf{H}(\text{div}, K)$. It is also important to highlight the following properties are satisfied by the basis functions in \mathbf{B}_k^K .

- The face functions $\Phi^{F,a} = \varphi^a \mathbf{v}^{F,a_s}$ vanish on the faces that do not have a as one of its vertices because the scalar functions φ^a verify this property. If a is a vertex of another face adjacent F by a , then the normal component of $\Phi^{F,a}$ restricted to it also vanishes, because $\mathbf{v}^{F,a}$ is parallel to this adjacent face. The normal component $\langle \Phi^{F,a}, \mathbf{n}^K \rangle|_F = \varphi^a|_F$, having in mind that the normal component of $\mathbf{v}^{F,a}$ is unitary over F .
- The face functions $\Phi^{F,l,n} = \varphi^{l,n} \mathbf{v}^{F,l}$ vanish on the faces that do not have l as one of its edges because the scalar functions $\varphi^{l,n}$ verify this property. Otherwise, the normal component of $\Phi^{F,l,n}$ restricted to a face adjacent to F by l vanishes, because $\mathbf{v}^{F,l}$ is parallel to it. Having in mind that the normal component of $\mathbf{v}^{F,l}$ is unitary over F , it follows that $\langle \Phi^{F,l,n}, \mathbf{n}^K \rangle|_F = \varphi^{l,n}|_F$.
- The face functions $\Phi^{F,n_1,n_2} = \varphi^{F,n_1,n_2} \mathbf{v}^{F,\perp}$ vanish on the faces different from F , because the scalar functions $\varphi^{F,n}$ have this property. Over F , the normal component $\langle \Phi^{F,n}, \mathbf{n}^K \rangle|_F = \varphi^{F,n_1,n_2}|_F$, having in mind that $\mathbf{v}^{F,\perp}$ coincides with the outward unit normal to F .

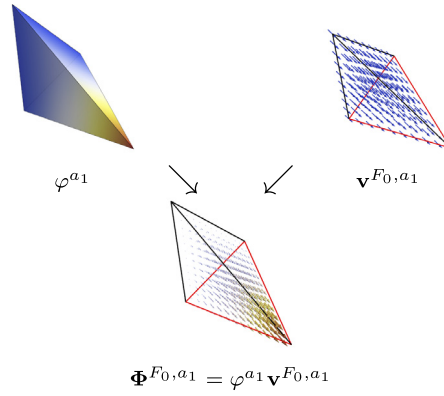


Fig. A.11. Illustration of the vectorial function $\Phi^{F_0,a_1} = \varphi^{a_1} \mathbf{v}^{F_0,a_1}$ for a tetrahedron (bottom side) which is obtained by the product of the vertex scalar function φ^{a_1} (top left side) by the vector field \mathbf{v}^{F_0,a_1} (top right side). The face F_0 is marked in red. (For interpretation of the references to colour in this figure legend, the reader is referred to the web version of this article.)

- The internal functions $\Phi^{K,l,n} = \varphi^{l,n} \mathbf{v}^{l,\top}$ vanish on all faces not sharing l , since the scalar function $\varphi^{l,n}$ satisfies this property. Otherwise, the normal component of $\Phi^{K,l,n}$ restricted to a face sharing l also vanishes, having in mind that $\mathbf{v}^{l,\top}$ is tangent to it.
- The internal functions $\Phi_{(j)}^{K,n_1,n_2,n_3} = \varphi^{K,n_1,n_2,n_3} \mathbf{v}_{(j)}^K$ vanish on all faces $F \in \mathcal{F}$, since the internal functions φ^{K,n_1,n_2,n_3} verify this property.

Observe that each scalar basis function in \mathcal{B}_k^K appears three times in the composition of the vectorial basis functions in \mathbf{B}_k^K , multiplied by three linearly independent vector fields. Precisely:

1. The vertex scalar functions φ^a , multiplied by the vector fields $\mathbf{v}^{F,a}$ of the three faces sharing the vertex a , appear in the composition of the face functions $\Phi^{F,a}$.
2. The edge scalar functions $\varphi^{l,n}$, multiplied by the field $\mathbf{v}^{F,l}$, appear in the composition of the face vectorial functions $\Phi^{F,l,n}$, associated to the two faces sharing l , and multiplied by the field $\mathbf{v}^{l,\top}$, they appear in the definition of the interior functions $\Phi^{K,l,n}$.
3. The face scalar functions φ^{F,n_1,n_2} , multiplied by the vectors $\mathbf{v}^{F,\perp}$, appear in the composition of the face vectorial functions Φ^{F,n_1,n_2} . Furthermore, multiplied by the vectors $\mathbf{v}_{(j)}^{F,\top}$, $j = 1, 2$, they compose the vectorial internal functions $\Phi_{(j)}^{K,F,n_1,n_2}$.
4. The internal scalar functions φ^{K,n_1,n_2,n_3} , multiplied by the vector fields $\mathbf{v}_{(j)}^K$ $j = 1, 2$ and 3 , appear in the composition of the three interior vector functions $\Phi_{(1)}^{K,n_1,n_2,n_3}$, $\Phi_{(2)}^{K,n_1,n_2,n_3}$, $\Phi_{(3)}^{K,n_1,n_2,n_3}$, respectively.

Theorem A.1. *The set of functions \mathbf{B}_k^K is linearly independent.*

Proof. Consider the linear combination

$$\begin{aligned}
 \mathbf{q} = & \sum_{F \in \mathcal{F}} \left[\sum_{a \in \mathcal{V}_F} \alpha_{F,a} \Phi^{F,a} + \sum_{l \in \mathcal{E}_F} \sum_n \beta_{F,l,n} \Phi^{F,l,n} + \sum_{n_1,n_2} \gamma_{F,n,n_2} \Phi^{F,n_1,n_2} \right] \\
 & + \sum_{l \in \mathcal{E}} \sum_n \theta_{l,n} \Phi^{K,l,n} + \sum_{F \in \mathcal{F}} \sum_{n_1,n_2} \left[\lambda_{F,n_1,n_2}^{(1)} \Phi_{(1)}^{K,F,n_1,n_2} + \lambda_{F,n_1,n_2}^{(2)} \Phi_{(2)}^{K,F,n_1,n_2} \right] \\
 & + \sum_{n_1,n_2,n_3} \left[\mu_{n_1,n_2,n_3}^{(1)} \Phi_{(1)}^{K,n_1,n_2,n_3} + \mu_{n_1,n_2,n_3}^{(2)} \Phi_{(2)}^{K,n_1,n_2,n_3} + \mu_{n_1,n_2,n_3}^{(3)} \Phi_{(3)}^{K,n_1,n_2,n_3} \right] = 0.
 \end{aligned}$$

The expression for \mathbf{q} can be rewritten by grouping the contributions of each of the scalar basis functions in \mathcal{B}_k^K :

$$\begin{aligned} \mathbf{q} = & \sum_{a \in \mathcal{V}} \left[\sum_{F \in \mathcal{F}_a} \alpha_{F,a} \mathbf{v}^{F,a} \right] \varphi^a + \sum_n \sum_{l \in \mathcal{E}} \left[\sum_{F \in \mathcal{F}_l} \beta_{F,l,n} \mathbf{v}^{F,l} + \theta_{l,n} \mathbf{v}^{l,\top} \right] \varphi^{l,n} \\ & + \sum_{F \in \mathcal{V}} \sum_{n_1, n_2} \left[\gamma_{F,n_1, n_2} \mathbf{v}^{F,\perp} + \lambda_{F,n_1, n_2}^{(1)} \mathbf{v}_{(1)}^{F,\top} + \lambda_{F,n_1, n_2}^{(2)} \mathbf{v}_{(2)}^{F,\top} \right] \varphi^{F, n_1, n_2} \\ & + \sum_{n_1, n_2, n_3} \left[\mu_{n_1, n_2, n_2}^{(1)} \mathbf{v}_{(1)}^K + \mu_{n_1, n_2, n_2}^{(2)} \mathbf{v}_{(2)}^K + \mu_{n_1, n_2, n_2}^{(3)} \mathbf{v}_{(3)}^K \right] \varphi^{K, n_1, n_2, n_3} = 0. \end{aligned}$$

The linear independence property of the scalar basis functions imply that the vector coefficients multiplying each of these functions appearing in the linear combination \mathbf{q} are zero. That is,

$$\sum_{F; a \in \mathcal{V}_F} \alpha_{F,a} \mathbf{v}^{F,a} = 0, \quad (\text{A.2})$$

$$\sum_{F \in \mathcal{F}_l} \beta_{F,l,n} \mathbf{v}^{F,l} + \theta_{l,n} \mathbf{v}^{l,\top} = 0, \quad (\text{A.3})$$

$$\gamma_{F,n_1, n_2} \mathbf{v}^{F,\perp} + \lambda_{F,n_1, n_2}^{(1)} \mathbf{v}_{(1)}^{F,\top} + \lambda_{F,n_1, n_2}^{(2)} \mathbf{v}_{(2)}^{F,\top} = 0, \quad (\text{A.4})$$

$$\mu_{n_1, n_2, n_2}^{(1)} \mathbf{v}_{(1)}^K + \mu_{n_1, n_2, n_2}^{(2)} \mathbf{v}_{(2)}^K + \mu_{n_1, n_2, n_2}^{(3)} \mathbf{v}_{(3)}^K = 0. \quad (\text{A.5})$$

Having in mind that the vector fields associated with each vertex of K are linearly independent, Eq. (A.2) implies that $\alpha_{F,a} = 0$. Similarly, the linear independency property of the three vector fields associated with each edge and Eq. (A.3) imply that $\beta_{F,l,n} = \theta_{l,n} = 0$. Eq. (A.4) and the linear independency property of the three vector fields associated with each face, imply that $\gamma_{F,n_1, n_2} = \lambda_{F,n_1, n_2}^{(1)} = \lambda_{F,n_1, n_2}^{(2)} = 0$. Finally, having in mind that the internal vector fields $\mathbf{v}_{(j)}^K$ form an orthonormal set, Eq. (A.5) implies that $\mu_{n_1, n_2, n_2}^{(1)} = \mu_{n_1, n_2, n_2}^{(2)} = \mu_{n_1, n_2, n_2}^{(3)} = 0$. Consequently, the set \mathbf{B}_k^K results to be linearly independent. ■

It should be observed that the vector fields considered in the definition of \mathbf{B}_k^K are not uniquely defined. However, the resulting space $\mathbf{P}_k = \text{span } \mathbf{B}_k^K$ is indeed unique. This can be deduced from the linear independency of the three vector fields associated to each basic element (vertex, edge, face or volume). As expressed in Eq. (A.2), the vectorial coefficients multiplying the scalar shape functions in the expansion for \mathbf{q} are unique. Consequently, dimension of \mathbf{P}_k should be 3 times the dimension of $P_k = \text{span } \mathcal{B}_k^K$, as can be verified in the last column of Table 1.

A.4. Approximation spaces in $\mathbf{H}(\text{div}, \Omega)$

Let \mathbf{q} be a vectorial function defined element-wise, on the elements of Γ , as $\mathbf{q}^K := \mathbf{q}|_K \in \text{span } \mathbf{B}_k^K \subset \mathbf{H}(\text{div}, K)$. In order to be a function in $\mathbf{H}(\text{div}, \Omega)$, the normal components of \mathbf{q} across the interfaces $F = K^\ell \cap K^j$ between two neighbouring elements K^ℓ and K^j should be continuous. As described next, this is an immediate consequence of the particular properties satisfied by the functions forming the vectorial bases \mathbf{F}_k^K , described in Appendix A.3, and of the continuity of the scalar shape functions across the interfaces F .

According to the properties satisfied by the basis functions in $\mathbf{B}_k^{K^\ell}$, the non-zero contributions to the normal component of \mathbf{q}^{K^ℓ} on the face F come from the face functions $\boldsymbol{\Phi}^{F,a}$, $\boldsymbol{\Phi}^{F,l,n}$ and $\boldsymbol{\Phi}^{F,n_1, n_2}$ associated with its vertices, edges and to the face itself. Precisely,

$$\langle \mathbf{q}^{K^\ell}, \mathbf{n}^{K^\ell} \rangle|_F = \sum_{a \in \mathcal{V}_F} \alpha_{F,a} \varphi^a|_F + \sum_{l \in \mathcal{E}_F} \sum_n \beta_{F,l,n} \varphi^{l,n}|_F + \sum_{n_1, n_2} \gamma_{F,n_1, n_2} \varphi^{F, n_1, n_2}|_F.$$

The jump on the normal component of \mathbf{q} across F is given by

$$[\langle \mathbf{q}^{K^\ell}, \mathbf{n}^{K^\ell} \rangle + \langle \mathbf{q}^{K^j}, \mathbf{n}^{K^j} \rangle]_F.$$

Assuming the continuity of the scalar basis functions across the interface F , and recalling that $\mathbf{n}^{K^j} = -\mathbf{n}^\ell$, this jump is zero if and only if in the expansions of \mathbf{q}^{K^ℓ} and \mathbf{q}^{K^j} the sum of the two coefficients multiplying each of the face functions associated with the vertices, edges and face of the interface F is zero. This result is summarized in the following theorem.

Theorem A.2. *Let Γ be a partition of the domain Ω by affine tetrahedra, hexahedral or prismatic elements K , and \mathbf{B}_k^K be the hierarchical basis (A.1). Consider a subspace \mathbf{V}_k^Γ of vectorial functions \mathbf{u} such that $\mathbf{q}^K = \mathbf{q}|_K \in \text{span } \mathbf{B}_k^K \subset \mathbf{H}(\text{div}, K)$. Suppose that for the expansions of \mathbf{q}^{K^ℓ} and \mathbf{q}^{K^j} , in terms of the bases $\mathbf{B}_k^{K^\ell}$ and $\mathbf{B}_k^{K^j}$ associated with two neighbouring elements $K^\ell, K^j \in \Gamma$ sharing a common face $F = K^\ell \cap K^j$, the sum of multiplying coefficients corresponding to each of the face functions associated with the vertices and edges of F , as well as to the face functions associated with the face F itself, is zero. Then \mathbf{V}_k^Γ is a subspace of $\mathbf{H}(\text{div}, \Omega)$.*

Appendix B. Local projections commuting the de Rham diagram

This part is dedicated to the study of the required local projections $\lambda_K \mathbf{q}$ verifying the commuting de Rham diagram property (9), for all spaces $\mathbf{M}(K)$ of type $\mathbf{P}_k(K)$, $\mathbf{P}_k^*(K)$ or $\mathbf{P}_k^{**}(K)$, described in Section 3. Let us recall the definitions for the spaces $D(K) = \nabla \cdot \mathbf{M}(K)$. Precisely, for tetrahedra, $D(K) = P_{k-1}(K)$ for the BDM_k spaces $\mathbf{M}(K) = \mathbf{P}_k(K)$. For all geometries, $D(K) = P_k(K)$ for spaces $\mathbf{M}(K) = \mathbf{P}_k^*(K)$, and $D(K) = P_{k+1}(K)$ when $\mathbf{M}(K) = \mathbf{P}_k^{**}(K)$. For all cases, the space

$$P(\partial K) = \left\{ \phi \in L^2(\partial K); \phi|_F \in P_k(F) \text{ on the faces } F \text{ of } K \right\}$$

represents the normal traces of functions in $\mathbf{M}(K)$. Consider direct decompositions $\mathbf{M}|(K) = \mathbf{M}_\partial(K) \oplus \mathring{\mathbf{M}}(K)$, where $\mathring{\mathbf{M}}(K) = \{ \sigma \in \mathbf{M}(K); \sigma \cdot \eta_K|_{\partial K} = 0 \}$ is the space of internal functions in $\mathbf{M}(K)$, $\mathbf{M}_\partial(K)$ being its complement.

As suggested in [27], let us consider factorizations $\lambda_K \mathbf{q} = \mathbf{q}_\partial + \mathring{\mathbf{q}}$, with boundary terms $\mathbf{q}_\partial \in \mathbf{M}_\partial(K)$, and internal terms $\mathring{\mathbf{q}} \in \mathring{\mathbf{M}}(K)$. The following observations are in order for the factorizations of different settings of $\mathbf{M}(K)$.

1. The boundary contributions \mathbf{q}_∂ can be computed in terms of the face shape functions in $\mathbf{P}_k(K)$, for all the cases.
2. The specifications for the internal contributions $\mathring{\mathbf{q}}$ depend on the specific space configuration adopted.

For the tetrahedral elements there are three settings:

1. $\mathbf{M}(K) = \mathbf{P}_k(K)$, $D(K) = P_{k-1}(K)$: for this case, denotes $\lambda_K = \rho_{k,K}$ for the classic BDM_k projection on $\mathbf{P}_k(K)$. Then $\mathring{\mathbf{q}} = \lambda_K(\mathbf{q} - \mathbf{q}_\partial) \in \mathbf{P}_k(K)$, with $\mathring{\mathbf{q}} \cdot \eta_K|_{\partial K} = 0$, can be computed in terms of the internal shape functions in $\mathbf{P}_k(K)$.
2. $\mathbf{M}(K) = \mathbf{P}_k^*(K)$ and $D(K) = P_k(K)$: in this case, let $\lambda_K = \rho_{k,K}^*$ be the classic $BDFM_{k+1}$ projection on $\mathbf{P}_k^*(K)$. Then, $\mathring{\mathbf{q}} = \mathring{\mathbf{q}}^* = \rho_{k,K}^*(\mathbf{q} - \mathbf{q}_\partial) \in \mathbf{P}_k^*(K)$ with $\mathring{\mathbf{q}}^* \cdot \eta_K|_{\partial K} = 0$. Since the internal spaces in $\mathbf{P}_k^*(K)$ and in $\mathbf{P}_{k+1}(K)$ coincide for tetrahedral elements, then this internal contribution can also be represented as $\mathring{\mathbf{q}}^* = \rho_{k+1,K}(\mathbf{q} - \mathbf{q}_\partial)$, in terms of the BDM_{k+1} projection on $\mathbf{P}_{k+1}(K)$, which can be expressed in terms of the internal shape functions of $\mathbf{P}_{k+1}(K)$.
3. $\mathbf{M}(K) = \mathbf{P}_k^{**}(K)$ and $D(K) = P_{k+1}(K)$: since for tetrahedral elements the three internal spaces in $\mathbf{P}_k^{**}(K)$, $\mathbf{P}_{k+1}^*(K)$ and $\mathbf{P}_{k+2}(K)$ coincide, for this particular setting we propose to define $\lambda_K = \rho_{k,K}^{**}$ as the projection such that $\mathring{\mathbf{q}}^{**} = \rho_{k+1,K}^*(\mathbf{q} - \mathbf{q}_\partial) = \rho_{k+2,K}(\mathbf{q} - \mathbf{q}_\partial)$, with $\mathring{\mathbf{q}}^{**} \cdot \eta_K|_{\partial K} = 0$. Thus, $\mathring{\mathbf{q}}^{**}$ can be computed by the $BDFM_{k+1}$ or by the BDM_{k+2} projections, meaning that it can be expressed by the internal shape functions of $\mathbf{P}_{k+2}(K)$.

For hexahedral and prismatic elements there are also different settings:

1. $\mathbf{M}(K) = \mathbf{P}_k^*(K)$ and $D(K) = P_k(K)$ for hexahedral elements: the projection $\lambda_K = \rho_{k,K}^*$ is taken by the classic RT_k projection, as proposed in [4], for which $\mathring{\mathbf{q}}^* = \rho_{k,K}^*(\mathbf{q} - \mathbf{q}_\partial) \in \mathbf{P}_k^*(K)$, with $\mathring{\mathbf{q}}^* \cdot \eta_K|_{\partial K} = 0$.
2. For prismatic elements, there exists the known Nédélec's setting $\mathbf{M}(K) = \mathbf{N}(K)$ such that $D(K) = P_k(K)$, and the same kind of trace space $P(\partial K)$. For this particular case, let us consider $\lambda_K = \rho_{k,K}^N$ as the projection introduced in [5].

3. $\mathbf{M}(K) = \mathbf{P}_k^*(K)$ and $D(K) = P_k(K)$ for prismatic elements: this framework shares with the previous Nédélec's setting the scalar spaces $D(K)$ and $P(\partial K)$, and consequently the boundary space $\mathbf{M}_\partial(K)$. However, $\mathring{\mathbf{M}}(K)$ strictly contains the internal Nédélec's functions. Therefore, a projection $\lambda_K = \rho_{k,K}^*$ on \mathbf{P}_k^* is still missing for prisms, but it shall be derived below.
4. $\mathbf{M}(K) = \mathbf{P}_k^{**}(K)$ and $D(K) = P_{k+1}(K)$, for hexahedral and prismatic elements: since the internal spaces in $\mathbf{P}_k^{**}(K)$ coincide with the corresponding internal spaces in $\mathbf{P}_{k+1}^*(K)$, and assuming projections $\rho_{k,K}^*$ being stated, then $\lambda_K = \rho_{k,K}^{**}$ is defined by taking $\mathring{\mathbf{q}}^{**} = \rho_{k+1,K}^*(\mathbf{q} - \mathbf{q}_\partial)$, with $\mathring{\mathbf{q}}^{**} \cdot \boldsymbol{\eta}_K|_{\partial K} = 0$, which can be expanded by the internal shape functions of $\mathbf{P}_{k+1}^*(K)$.

Finally, it remains to derive $\lambda_K = \rho_{k,K}^*$ for the case $\mathbf{M}(K) = \mathbf{P}_k^*(K)$ and $D(K) = P_k(K)$ for prismatic elements. Let it be defined by the factorization $\rho_{k,K}^* \mathbf{q} = \mathbf{q}_\partial + \mathring{\mathbf{q}}^*$ whose components verify the relations

$$\int_{\partial K} \mathbf{q}_\partial \cdot \boldsymbol{\eta}_K \phi ds = \int_{\partial K} \mathbf{q} \cdot \boldsymbol{\eta}_K \phi ds, \quad \forall \phi \in P(\partial K), \quad (\text{B.1})$$

$$\int_K \nabla \cdot \mathring{\mathbf{q}}^* \nabla \cdot \boldsymbol{\sigma} dK = \int_K \nabla \cdot \mathbf{q} \nabla \cdot \boldsymbol{\sigma} dK, \quad \forall \boldsymbol{\sigma} \in \mathring{\mathbf{M}}(K), \nabla \cdot \boldsymbol{\sigma} \neq 0, \quad (\text{B.2})$$

$$\int_K \mathring{\mathbf{q}}^* \cdot \boldsymbol{\sigma} dK = \int_K \mathbf{q} \cdot \boldsymbol{\sigma} dK, \quad \forall \boldsymbol{\sigma} \in \mathring{\mathbf{M}}(K), \nabla \cdot \boldsymbol{\sigma} = 0. \quad (\text{B.3})$$

This is the form in which the projections in [27] are presented, for hp finite element spaces, and in Appendix B of [28], for the case of Raviart–Thomas spaces of variable degree on a simplex.

Uniqueness of the projection $\rho_{k,K}^* \mathbf{q}$ is an immediate consequence of the conditions (B.1)–(B.3) by assuming zero right hand sides. From Eq. (B.1), assuming $\mathbf{q} \cdot \boldsymbol{\eta}_K|_{\partial K} = 0$, it follows that $\mathbf{q}_\partial \cdot \boldsymbol{\eta}_K|_{\partial K} = 0$, meaning that $\mathbf{q}_\partial = 0$. It is also clear that $\mathring{\mathbf{q}}^* \in \mathring{\mathbf{M}}(K)$ verifying Eqs. (B.2)–(B.3) with vanishing right hand sides is only possible if $\mathring{\mathbf{q}}^* = 0$.

Local de Rham commuting diagram

Except for the projections referring to prismatic elements $\mathbf{M}(K) = \mathbf{P}_k^*(K)$ and $D(K) = P_k(K)$, and for the settings $\mathbf{M}(K) = \mathbf{P}_k^{**}(K)$ and $D(K) = P_{k+1}(K)$ of all element geometries, the projections $\lambda_K \mathbf{q}$ for the other ones are known to verify the local de Rham commuting property

$$\int_K \nabla \cdot \lambda_K \mathbf{q} \varphi dK = \int_K \nabla \cdot \mathbf{q} \varphi dK, \quad \forall \varphi \in D(K). \quad (\text{B.4})$$

The case $\lambda_K \mathbf{q} = \rho_{k,K}^* \mathbf{q}$ for prismatic elements: It has been defined by the statements (B.1)–(B.3). Following the suggestion in [28], first observe that for constant $\varphi = 1$, the relation (B.4) follows from the first statement (B.1). That is,

$$\int_K \nabla \cdot (\lambda_K \mathbf{q} - \mathbf{q}) dK = \int_{\partial K} (\lambda_K \mathbf{q} - \mathbf{q}) \cdot \boldsymbol{\eta} ds = \int_{\partial K} (\mathbf{q}_\partial - \mathbf{q}) \cdot \boldsymbol{\eta} ds = 0.$$

Because of this result, it is sufficient to prove (B.4) for $\varphi \in D(K)$ with zero mean, and $\varphi \neq 0$. Suppose that for such functions there exist $\boldsymbol{\sigma} \in \mathring{\mathbf{M}}(K)$ with $\nabla \cdot \boldsymbol{\sigma} = \varphi$. Thus, from (B.2) we obtain

$$\int_K \nabla \cdot (\lambda_K \mathbf{q} - \mathbf{q}) \varphi dK = \int_K \nabla \cdot (\lambda_K \mathbf{q} - \mathbf{q}) \nabla \cdot \boldsymbol{\sigma} dK = 0.$$

To prove the surjection property of the divergence operator, for $\varphi \in D(K)$ with zero mean, and $\varphi \neq 0$, consider the smooth function u satisfying $\Delta u = \varphi$ on K , and $\nabla u \cdot \boldsymbol{\eta}_K = 0$ on ∂K . Define $\boldsymbol{\sigma} = \mathring{\mathbf{q}}^N = \lambda_K^N \nabla u$ as the Nédélec's projection of $\mathbf{q} = \nabla u$ on $\mathbf{N}_K(K)$. It verifies $\mathring{\mathbf{q}}^N \cdot \boldsymbol{\eta}_K|_{\partial K} = \nabla u \cdot \boldsymbol{\eta}_K|_{\partial K} = 0$, and $\int_K (\mathring{\mathbf{q}}^N - \nabla u) \cdot \mathbf{r} dK = 0$ for all $\mathbf{r} \in \Psi_k(K)$, where $\Psi_k(K)$ represents the image of $D(K)$ by the gradient operator. Therefore, $\mathring{\mathbf{q}}^N$ is indeed an internal function in $\mathring{\mathbf{N}}_K(K) \subsetneq \mathring{\mathbf{M}}(K)$. To see that $\nabla \cdot \mathring{\mathbf{q}}^N = \varphi$, use Green's formula to obtain for all $s \in D(K)$

$$\int_K \nabla \cdot \mathring{\mathbf{q}}^N s dK = - \int_K \mathring{\mathbf{q}}^N \cdot \nabla s dK = - \int_K \nabla u \cdot \nabla s dK = \int_K \varphi s dK.$$

The cases $\lambda_K \mathbf{q} = \rho_{k,K}^{} \mathbf{q}$ for all element geometries:** They are associated with the settings $\mathbf{M}(K) = \mathbf{P}_k^{**}(K)$ and $D(K) = P_{k+1}(K)$. Applying the definition $\rho_{k,K}^{**} \mathbf{q} = \mathbf{q}_{\partial+K}^{**}$, where $\mathbf{q}^{**} = \rho_{k+1,K}^*(\mathbf{q} - \mathbf{q}_\partial)$, we obtain $\nabla \cdot \rho_{k,K}^{**} \mathbf{q} = \nabla \cdot \mathbf{q}_{\partial+K}^* \cdot \rho_{k+1,K}^*(\mathbf{q} - \mathbf{q}_\partial)$. Since $\mathbf{q}_\partial \in \mathbf{P}_k$, and then $\nabla \cdot \mathbf{q}_\partial = \pi_{k+1,K} \nabla \cdot \mathbf{q}_\partial$, and using the commuting de Rham property $\rho_{k+1,K}^* \nabla \cdot \rho_{k+1,K}^*(\mathbf{q} - \mathbf{q}_\partial) = \pi_{k+1,K} \nabla \cdot (\mathbf{q} - \mathbf{q}_\partial)$, which is valid for all projections $\rho_{k+1,K}^*$ associated to the settings $\mathbf{M}_{k+1}(K) = \mathbf{P}_{k+1}^*(K)$ and $D_{k+1}(K) = P_{k+1}(K)$, then the desired commuting property also holds for $\rho_{k,K}^{**} \mathbf{q}$ as well.

References

- [1] F. Brezzi, M. Fortin, Mixed and Hybrid Finite Element Methods, in: Springer Series in Computational Mathematics, vol. 15, Springer-Verlag, New York, 1991.
- [2] P.A. Raviart, J.M. Thomas, A mixed finite element method for 2nd order elliptic problems, Lect. Note Math. 606 (1977) 292–315.
- [3] F. Brezzi, J. Douglas, L.D. Marini, Two families of mixed finite elements for second order elliptic problems, Numer. Math. 47 (1985) 217–235.
- [4] J.C. Nédélec, Mixed finite elements in \mathbb{R}^3 , Numer. Math. 35 (1980) 315–341.
- [5] J.C. Nédélec, A new family of mixed finite elements in \mathbb{R}^3 , Numer. Math. 50 (1986) 57–81.
- [6] F. Brezzi, J. Douglas Jr., R. Durán, M. Fortin, Mixed finite elements for second order elliptic problems in three variables, Numer. Math. 51 (1987) 237–250.
- [7] F. Brezzi, J. Douglas, M. Fortin, L.D. Marini, Efficient rectangular mixed finite elements in two and three space variable, RAIRO Modél. Math. Anal. Numér. 2 (1987) 581–604.
- [8] P. Solin, K. Segeth, I. Dolezel, Higher-Order Finite Element Methods, Chapman - Hall/CRC, 2004.
- [9] L. Demkowicz, Polynomial exact sequence and projection-based interpolation with application Maxwell equations, in: D. Boffi, L. Gastaldi (Eds.), Mixed Finite Elements, Compatibility Conditions and Applications, 2006, pp. 101–156.
- [10] S. Zaglamayr, High order finite element methods for electromagnetic field computation (Ph.D. thesis), Johannes Kepler Universität Linz, 2006.
- [11] A. Buffa, G. Sangalli, R. Vázquez, Isogeometric analysis in electromagnetics: B-splines approximation, Comp. Methods Appl. Mech. Engrg. 199 (2010) 1143–1152.
- [12] W. Qiu, L. Demkowicz, Mixed hp -finite element method for linear elasticity with weakly imposed symmetry III: stability analysis in 3D, SIAM J. Numer. Anal. 49 (2011) 619–641.
- [13] F. Fuentes, B. Keith, L. Demkowicz, S. Nagaraj, Orientation embedded high order shape functions for the exact sequence elements of all shapes, Comput. Math. Appl. 70 (2015) 353–458.
- [14] D.N. Arnold, R.S. Falk, R. Winther, Finite element exterior calculus, homological techniques, and applications, Acta Numer. 15 (2006) 1–155.
- [15] D.N. Arnold, G. Awanou, Finite element differential forms on cubical meshes, Math. Comp. 83 (2014) 1551–1570.
- [16] M.E. Rognes, R.C. Kirby, A. Logg, Efficient assembly of $H(\text{div})$ and $H(\text{curl})$ conforming finite elements, SIAM J. Sci. Comput. 31 (6) (2009) 4130–4151.
- [17] D.N. Arnold, D. Boffi, R.S. Falk, Quadrilateral $H(\text{div})$ finite elements, SIAM J. Numer. Anal. 42 (6) (2005) 2429–2451.
- [18] T. Arbogast, M.R. Correa, Two Families of $H(\text{div})$ Mixed Finite Elements on Quadrilaterals of Minimal Dimension, ICES REPORT 15-09, The Institute for Computational Engineering and Sciences, The University of Texas at Austin, 2015, March.
- [19] R. Araya, C. Harder, D. Paredes, F. Valentin, Multiscale hybrid-mixed method, SIAM J. Numer. Anal. 51 (2013) 3505–3531.
- [20] D. Siqueira, P.R.B. Devloo, S.M. Gomes, A new procedure for the construction of hierarchical high order $H(\text{div})$ and $H(\text{curl})$ finite element spaces, J. Comput. Appl. Math. 240 (2013) 204–214.
- [21] P.R.B. Devloo, A.M. Farias, S.M. Gomes, D. Siqueira, Two-dimensional hp adaptive finite element spaces for mixed formulations, Math. Comput. Simulat. (2016) in press, <http://dx.doi.org/10.1016/j.matcom.2016.03.009>.
- [22] NeoPZ: <http://github.com/labmec/neopz>.
- [23] A.M. Farias, Novas Formulações de Elementos Finitos e Simulações Multifísicas (Doctorate thesis), IMECC-Unicamp, 2014.
- [24] P.R.B. Devloo, C.M.A. Bravo, C.M.A. Rylo, Systematic and generic construction of shape functions for p -adaptive meshes of multidimensional finite elements, Comput. Meth. Appl. Mech. Engrg. 198 (2009) 1716–1725.
- [25] J.L.D. Calle, P.R.B. Devloo, S.M. Gomes, Implementation of continuous hp -adaptive finite element spaces without limitations on hanging sides and distribution of approximation orders, Comput. Math. Appl. 70 (5) (2015) 1051–1069.
- [26] D.A. Castro, P.R.B. Devloo, A.M. Farias, S.M. Gomes, O. Durán, Hierarchical high order finite element bases for $H(\text{div})$ spaces based on curved meshes for two-dimensional regions or manifolds, J. Comput. Appl. Math. 301 (2016) 241–258.
- [27] L. Demkowicz, P. Monk, L. Vardapetvan, W. Rachowicz, De Rham diagram for hp finite element spaces, Comput. Math. Appl. 39 (2000) 29–38.
- [28] B. Cockburn, J. Gopalakrishnan, Error analysis of variable degree mixed methods for elliptic problems via hybridization, Math. Comp. 74 (252) (2005) 1653–1677.